UNIVERSITY OF CALIFORNIA

Los Angeles

Dissertation Title

A dissertation submitted in partial satisfaction

of the requirements for the degree

Doctor of Philosophy in Mechanical Engineering

by

Jon Thomas Van Lew

2015

ABSTRACT OF THE DISSERTATION

Dissertation Title

by

Jon Thomas Van Lew

Doctor of Philosophy in Mechanical Engineering

University of California, Los Angeles, 2015

Professor Mohamed Abdou, Chair

It's all crap

The dissertation of Jon Thomas Van Lew is approved.

member 3

member 2

member 1

Mohamed Abdou, Committee Chair

University of California, Los Angeles

2015

Table of Contents

LIST OF FIGURES

List of Tables

a	lattice parameter,
A	sample cross-sectional area, m^2
A_s	sample surface area, m^2
b	sample thickness, m
Bi	Biot number $(=hb/k)$
c_p	specific heat, J/kg·K
C	capacitance, F
D	electric displacement, C/m^2
d_{33}	piezoelectric coefficient, C/N
Δh	specific phase change enthalpy, J/kg
E	electric field, V/m
E_{br}	electrical breakdown field, V/m
E_c	coercive electric field, V/m
f	frequency, Hz
g	gravity of Earth $(=9.81$ m/s$^2)$
h	heat transfer coefficient, W/m^2·K
k	thermal conductivity, W/m·K
I_p	electric current, A
M$_A$	monoclinic M$_A$ crystal phase
M$_B$	monoclinic M$_B$ crystal phase
M$_C$	monoclinic M$_C$ crystal phase
$mol\%$	molar fraction, %
MPB	morphotropic phase boundary
N_D	energy density, J/L
Nu	Nusselt number
O	orthorhombic crystal phase

p_c	pyroelectric coefficient, C/m²·K
P	polarization density, C/m²
P_D	power density, W/L
P_r	remnant polarization, C/m²
P_s	saturation polarization, C/m²
Q	charge, C
Q_{in}	thermal energy input per unit volume, J/m³
PE	pyroelectric element
R	rhombohedral crystal phase
R	resistance, Ω
Ra	Rayleigh number
S	side length, m
s_{33}	elastic compliance, m²/N
t	time, s
T	tetragonal crystal phase
T	temperature, ^{o}C or K
T_{Curie}	Curie temperature, ^{o}C
x	molar fraction of lead titanate, %
x_3	strain in longitudinal direction $[=\int_{T_C}^{T}\alpha(T)\,\mathrm{d}T]$
$\cancel{V}$	volume, m³
V	voltage, V
V_1	voltage across capacitor, V
V_2	voltage across resistor, V
W_{in}	mechanical energy input per unit volume, J/m³

Greek symbols

α	linear thermal expansion coefficient, K⁻¹
δ	relative error between experimental data and model predictions, %

ε_o	vacuum permittivity ($= 8.854\text{x}10^{-12}$ F/m)
ε_r	relative permittivity
η	material efficiency, %
ν	kinematic viscosity, m^2/s
ρ	density, kg/m^3
σ	elastic stress, Pa
τ_t	thermal characteristic time constant, s
τ_{ij}	duration of process i-j, s

Subscripts

avg	refers to average
b	refers to bias
$cold$	refers to cold
eff	refers to effective
f	refers to fluid
H	refers to high
hot	refers to hot
L	refers to low
max	refers to maximum
PE	refers to pyroelectric element

Acknowledgments

I did it all on my own

Vita

2005	B.S., Mechanical Engineering, Cum Laude University of Arizona Tucson, AZ
2010	M.S., Mechanical Engineering University of Arizona Tucson, AZ

CHAPTER 1

Introduction

Lithiated ceramic pebbles have been chosen by many participants in ITER experiments as a material to be used for tritium generation.[?,?,?,?] Adjustments in the manufacturing processes of the ceramic pebbles permits variation of characteristics such as the pebble's tritium retention and release properties, lithium density, opened- and closed-porosity, nominal diameter, and crush strength. The variations are often coupled. For instance, for the sake of tritium management the open porosity is often increased which comes at the expensive of a decreased crush strength of the pebble. Because of the relatively weak crush strength distributions among batches of pebbles as well as the value of stresses predicted in the pebble bed, it is inevitable that during operation in the fusion environment individual pebbles will 'fail' in the ensemble. Designers of lithium ceramic tritium breeding blankets must mitigate pebble failure but also anticipate the breadth and magnitude of effects that some unavoidable failure will have on macroscopic properties.

To develop a complete numerical model for a pebble bed requires completing many interactive sub-models. To demonstrate, we give here the path of a possible analysis scheme of these models. To begin, one must have knowledge of the interaction of the pebble bed with the containing structure as they exist in a fusion environment. The interactions are generally analyzed via the finite element method to find internal stresses and temperature fields of the entirety of the pebble bed. After the internal fields are mapped, one would use the discrete element method (DEM) to interpret the macro-scopic stress fields into the inter-particle forces. With the inter-particle forces and total absorbed thermal energy calculated, a prediction of the initiation of pebble failure would predict the number of pebbles (if any)

that would be crushed in that computational volume. When a pebble is crushed, it loses contact with its neighbors and subsequently breaks any thermal or mechanical transport that the pebble was providing. Fragmentation of a failed pebble would also be handled by the DEM with another model. Following this, DEM would determine how the pebble bed re-settles and effective properties evolve in the presence of failed pebbles. Finally, the updated bed properties would feed back into the FEM formulation to predict how overall stress fields and material interactions are altered in light of the failure. The fusion community is far from an integrated simulation that can follow such a path, but it is the principle goal of the overall efforts at UCLA.

Research on pebble failure up to now has focused on predicting when pebbles may fail in a bed as a function of an external load (typically, stress from walls). In this study, we analyze the evolution of pebble bed properties assuming some fraction of pebbles in the ensemble have failed. The focus of this study is to determine the extent of change in aggregate ensemble properties due to individual pebble failure, as well as help designers anticipate acceptable limits of pebble failure from a thermal-management point of view. We make use of DEM to simulate individual pebbles in a packed bed. From this scale of simulation, we can study single pebbles undergoing failure while the bed as a whole is subject to mechanical and thermal boundaries.

For the DEM tools used in this study, the only mode of heat transfer is conduction through the solids. In a fusion breeder however, the helium purge gas winding through the interstitial gaps of the pebbles will have a large contribution to overall heat transfer.[?,?] To overcome the current limit on DEM heat transfer, we are also working with computational fluid dynamics coupling to the discrete element method to account for the helium energy transport. The next step is to combine our analysis tools with a failure initiation predictor as well as a new method of simulating a pebble after failure. Those modeling enhancements will be reported in the future. As these models become more comprehensive in their scope, the fusion community will be better prepared to determine the survivability and performance of a solid breeder design in the fusion environment.

The discrete element method (DEM) is used by many ceramic breeder researchers to model the interaction of individual pebbles in an ensemble in an effort to obtain a more detailed understanding of pebble beds than is possible with experimental measurements of effective properties. For example see Refs.[?,?,?,?,?,?] A major assumption in the DEM formulation is that each pebble acts perfectly elastically and adheres to Hertz theory for contacting spheres. With Hertz theory, one finds contact forces as a simple function of: the virtual overlap between two objects, the Young's modulus of the contacting material (and Poisson ratio), and radii of the two. In past studies, the Young's modulus of the ceramic materials used in DEM simulations was taken from historical data, for instance lithium metatitanate from Ref.[?]

Based on observations of experimental data from single pebble crush data, in this study we propose a new method of obtaining the Young's modulus for a batch of ceramic pebbles as the historical values from literature are not always appropriate.

The solid breeder in many current designs for ITER feature sub-module units of packed beds1. From the point of view of pebble bed thermomechanics, this has the advantage of producing units individually that can be tested and qualified to desired packing states (and therefore thermomechanics) during the design phase. We aim to provide designers of packed beds with tools to understand how packing states may evolve from time-dependent phenomena (e.g. sintering, creep, pebble cracking, etc.). These phenomena may, for instance: decrease the effective thermal conductivity which will raise bed temperatures beyond initial predictions, produce isolated pebbles which will sinter and potentially decrease tritium release rates, or even the form gaps between pebble beds and containing structures leading to divergence from initial packing properties. Modeling research on ceramic pebble beds should have as its main objective a thorough understanding of the evolution of pebble bed morphology and the impact on thermophysical properties; allowing for temperature control of breeder pebble beds over the entire lifetime of the blanket. To accomplish that goal, this current study is aimed at developing a methodology for coupling established discrete element models of individual pebbles in the ensemble with thermo-fluid simulations of the interstitial

helium purge gas. Specifically, we will address the impact of helium on the thermal transport in a bed experiencing evolving morphology due to cracked pebbles. Global models of pebble beds and helium flow with pebble-scale detail are intractable with current computational hardware and modeling techniques. To overcome deficiencies in computational power, we introduce two new modeling approaches that allow us to resolve pebble-scale interactions with bed-scale conjugate heat transfer with flowing gas.

CHAPTER 2

Pebble Interaction Analysis: Theory

This chapter will walk through the analysis first performed by Heinrich Hertz in 1880 of idealized interacting spherical objects to represent our ceramic pebbles. We will begin with mechanical interactions of purely elastic spheres and then use the results to develop a theory for conductive heat transfer between the pebbles. Finally, Hertz's theory will also be used to analyze pebble interaction with flat plattens in our test stand used to measure crush force. A relationship is developed allowing us to translate from experimental results to pebble bed ensembles.

2.1 Hertz theory for normal contact of spheres

[DRAW SOME COORDINATE DIAGRAMS TO SHOW HOW Z R AND X-Y WHAT-EVER ARE ACTUALLY RELATED AND CAN BE VISUALIZED] We consider two non-conforming solids approaching and then contacting under load. We only wish to analyze the contact of spheres (of differeng radii), so we are able define the surface curvature of the two contacting bodies as

$$z_1 = \frac{1}{2R_1}r^2 \tag{2.1}$$

$$z_2 = \frac{1}{2R_2}r^2 \tag{2.2}$$

respectively. The radius, laying in the $x - y$ plane is related to cartesian coordinates as $r^2 = x^2 + y^2$. Before the surfaces are in contact, each point on the two surfaces are separated by a distance $h(r)$,

$$h = z_1 - z_2$$

$$h = \left(\frac{1}{R_1} + \frac{1}{R_2} \right) \frac{r^2}{2} \tag{2.3}$$

We define the relative radius of curvature as

$$\frac{1}{R^*} = \frac{1}{R_1} + \frac{1}{R_2} \tag{2.4}$$

and then the separation is simply $h = (1/2R^*)r^2$.

We allow the two surfaces to approach, and then, under an external load F, contact. The cross-section of these bodies after contact are shown in Fig. 2.1. If we first imagine that the two surfaces do not interact and their surfaces pass through each other unimpeded, their surfaces would be overalapped to a distance δ. In such a case, we examine two points deep within the bodies, along the axis of contact, calling them T_1 and T_2. These points will have moved δ_1 and δ_2, respectively. The total overlap is obviously related to these displacements by $\delta = \delta_1 + \delta_2$.

However, under actual contact, the two surfaces are going to deform as the load F presses them into contact. So now we consider two points on the surfaces, such as S_1 and S_2. Before contact, these two points are initially are separated by a distance h (from Eq. 2.3), then displace by $\bar{u}_{z1}$ and $\bar{u}_{z2}$ due to contact pressure.

If the points S_1 and S_2 are inside of the contact region under load, these distances are related by

$$\bar{u}_{z1} + \bar{u}_{z2} + h = \delta \tag{2.5}$$

Then using Eq. 2.3, we have an expression for the elastic displacements:

$$\bar{u}_{z1} + \bar{u}_{z2} = \delta - \frac{1}{2R^*} r^2 \tag{2.6}$$
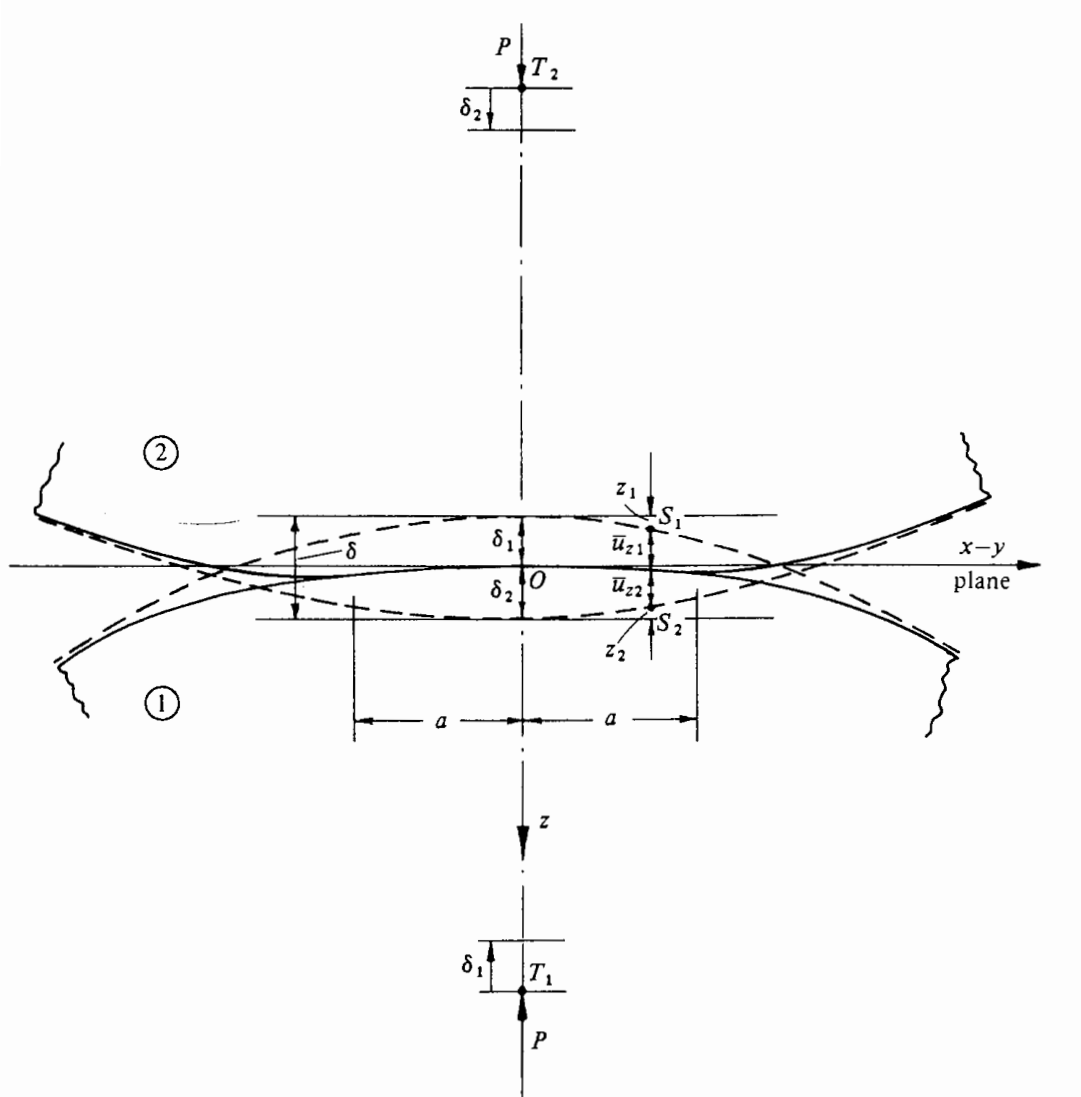
Figure 2.1: default

Alternatively, if after deformation the points S_1 and S_2 are outside of the contact region, this is simply

$$\bar{u}_{z1} + \bar{u}_{z2} > \delta - \frac{1}{2R^*} r^2 \qquad (2.7)$$

It now is necessary to find a pressure distribution that satisfies these boundary conditions of displacement. Heinrich Hertz first formulated the expressions of Eqs. **??** in 1882. The

power of his solution is borne out by the continuous use of his theory since that time. Hertz simplified the problem by regarding each body as an elastic half-space upon which the load is applied over a small, elliptical region (the contact area). This simplification allows for treatment of the highly concentrated stresses near the region of contact without consideration of either the general response of stresses in the bulk of the body or the manner in which they are supporting the load. This assumption is justifiable if the dimensions of each body as well as the relative radii of curvature are very large compared to the contact area. These assumptions are sufficient to proceed with the analysis, but the curious are pointed to an excellent discussion and background of Hertz's theory as given in KE Johnson's textbook.[?]

For solids of revolution, a distribution of pressure to satisfy the displacements of Eq. **??** is proposed by Hertz as

$$p = p_0 \left[1 - \left(\frac{r}{a} \right)^2 \right]^{1/2} \tag{2.8}$$

where a is the radius of the contact area.

The total load, F is found from the pressure distribution as

$$F = \int_0^a p(r) 2\pi r \, \mathrm{d}r \tag{2.9}$$

$$F = \frac{2}{3} p_0 \pi a^2 \tag{2.10}$$

From the distributed load over the circular region, stresses and deflections are found from superposition of point loads. The pressure is integrated (see Ref.[?]) to find the normal displacement for either solid body as

$$\bar{u}_z = \frac{1 - \nu^2}{E} \frac{\pi p_0}{4a} \left(2a^2 - r^2 \right) \tag{2.11}$$

This is applied to both bodies and plugged into Eq. 2.6 to yield

$$\frac{\pi p_0}{4aE^*} \left(2a^2 - r^2\right) = \delta - \left(\frac{1}{2R^*}\right) r^2 \tag{2.12}$$

where we have introduced the now-common term of pair Young's modulus,

$$\frac{1}{E^*} = \frac{1 - \nu_1^2}{E_1} + \frac{1 - \nu_2^2}{E_2} \tag{2.13}$$

for simplification.

With the solution of Eq. 2.12, if we consider $r = a$ and $\delta(a) = 0$, we find the radius of the contact circle is

$$a = \frac{\pi p_0 R^*}{2E^*} \tag{2.14}$$

and when $r = 0$, we find the overlap as

$$\delta = \frac{\pi a p_0}{2E^*} \tag{2.15}$$

and alternatively we find the pressure as a function of overlap

$$p_0 = \frac{2E^* \delta}{\pi a} \tag{2.16}$$

The radius, overlap, and pressure relations are inserted into Eq. 2.9 to find the force (from now on referred to as the Hertz force) as a function of overlap, relative radius, and pair Young's modulus,

$$F = \frac{4}{3} E^* \sqrt{R^*} \, \delta^{3/2} \tag{2.17}$$

Equation 2.17 defines the normal contact forces between any two contacting, elastic spheres. This extremely important result acts as the basis of all discrete element method codes since the concept was first introduced for granular materials by Cundall & Strack in

1979.[?] To differentiate the force from other terms to be derived later, we specificy it as the normal force between sphere i and sphere j as

$$F_{n,ij} = \frac{4}{3} E_{ij}^* \sqrt{R_{ij}^*}\, \delta_{ij}^{3/2} \tag{2.18}$$

CHAPTER 3

Pressure drop across packed beds

CHAPTER 4

Heat transfer in packed beds

This section covers a discussion of different modes of heat transfer experienced by a pebble in a packed bed. The main modes are conduction to neighbors and convection.

4.1   Single particle modes of heat transfer

The transient energy balance for an irradiated pebble, shown in Fig. 4.1, in a packed bed with flowing interstitial gas is given by Eq. 4.1,

$$\rho V C \frac{\mathrm{d}T}{\mathrm{d}t} = \dot{Q}_g + Q_{\text{conduction}} + \dot{Q}_{\text{convection}} + \dot{Q}_{\text{radiation}} \tag{4.1}$$

We begin with the lumped capacitance assumption that internal temperature gradients inside of the solid particle are negligible thus we can neglect diffusion terms in the solid. The validity of that assumption for the ceramic pebbles in fusion reactors will be discussed in detail in §**??**. The terms on the right-hand-side of Eq. 4.1 are:

1. rate of energy generated internal to the pebble,

2. rate of conduction between neighboring pebbles in their regions of contact,

3. rate of convective heat transfer with the interstitial helium gas (which includes energy carried far downstream or redeposited to neighboring pebbles), and

4. rate of radiative exchange between local solids.

Figure 4.1: Each ceramic pebble in a fusion reactor will experience multiple modes of heat transfer.
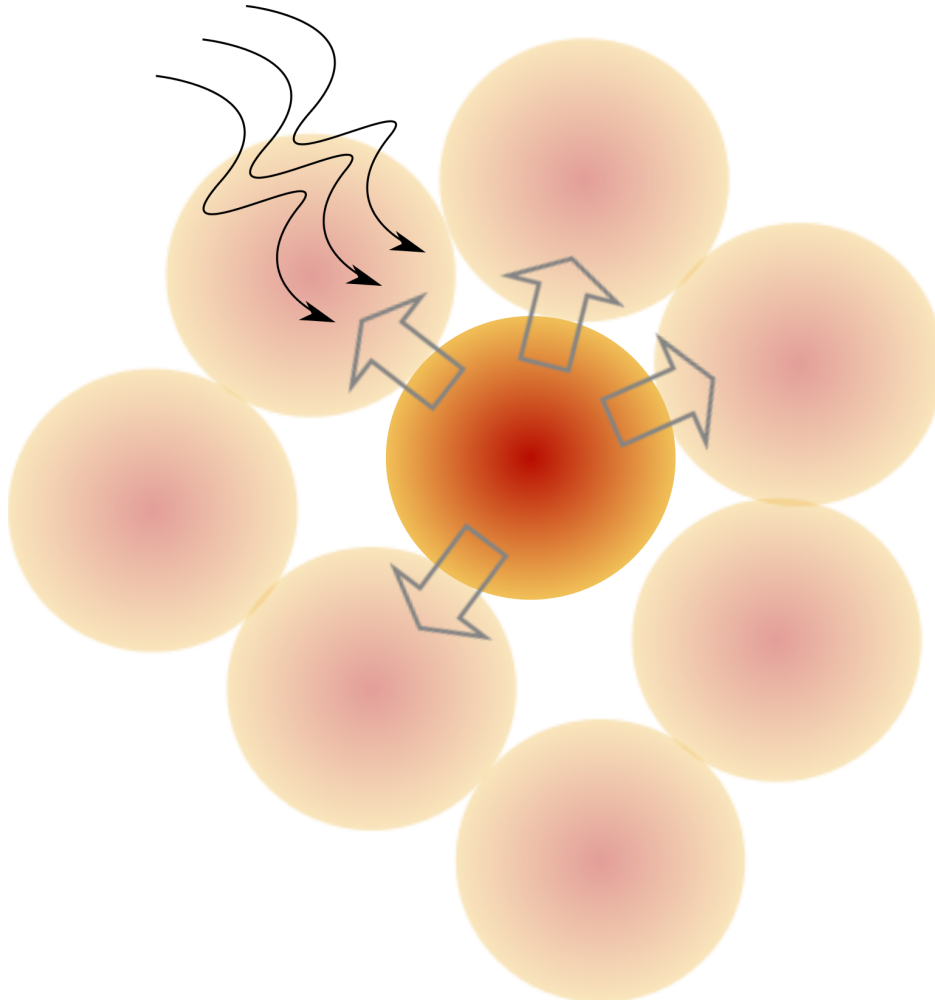
In this section we will provide a brief overview of all the modes of heat transfer to provide an overview of the importance and impact of each mode. For cases when more detail is needed, the details will be expounded in their own complete sections.

4.1.1 Heat generation

Nuclear deposition of energy is handled in a straightforward manner. With a known volumetric energy generation rate, q''' prescribed by, for instance, the neutron heating in the volume, the heat generation rate for this particle is simply

$$\dot{Q}_g = q'''V \tag{4.2}$$

4.1.2 Conduction with neighboring particles

When the particle is in contact with neighboring particles of differing temperature, they will transfer energy via conduction. If we begin by considering just two isothermal particles, we may employ a heat conductance term, h_c, to generically quantify the ease of energy movement between the two particles. In that case, the rate of heat transferred between the particles is written as

$$\dot{Q}_{\text{conduction, 1-2}} = h_c(T_1 - T_2) \tag{4.3}$$

where the heat conductance has units of W/K, not to be confused with the units of the heat transfer coefficient employed in convective heat trasnfer. Obviously this same term may be applied to all contacting neighbors such that the total rate of energy transfer due to conduction can be generically written as

$$\dot{Q}_{\text{conduction}} = \sum_{\forall \text{contacts}} \dot{Q}_{\text{conduction,1-contact}} h_c(T_1 - T_{\text{contact}}) \tag{4.4}$$

Of course, we must be careful with the application of this summation. We are assuming that a particle's interaction with each neighbor proceeds indepedently and thus their results can be superimposed. Furthermore, we have not given a means of calculating the heat conductance, h_c. These issues will be addressed more completely in §4.2.

4.1.3 Convection by interstitial gas

Engineers have paid considerable attention to the calculation of convective heat transfer in packed beds. Correlations for determining the Nusselt number of a sphere in dilute and dense packings over a range of Reynolds and Prandtl number are available. We will cover

the detail of many of these correlations in §**??**. The methods all come down to calculating Nusselt number to find the heat transfer coefficient and then computing the rate of heat transfer from convection as

$$\dot{Q}_{\text{convection}} = -hA(T_s - T_f) \tag{4.5}$$

where T_s is the temperature of the solid with surface area, A, and T_f is the average bulk temperature of the passing fluid. The negative sign is to maintain convention that energy transfer into the solid is positive.

4.1.4 Radiative transfer with neighboring particles

The radiation exchange between contacting neighbors becomes excessively complex in a packed bed due to the local and semi-local nature of radiation. A standard approach to radiation exchange between surfaces is to consider the view factor between them. In a dense, randomly packed bed of spheres the computation of view factors between pebbles can be done via a method such as that proposed Feng and Han.[?]

4.2   Inter-particle conduction

[Go back through Batchelor and O'Brien[?] paper]

$$\frac{k_s}{k_f} \frac{a}{R^*} = \lambda \tag{4.6}$$

Similar to the lumped capacitance assumptions, if $\lambda \gg 1$, the solid is approximately is isothermal. The second group on the left-hand side of this condition we remember from the assumptions of Hertz theory, where we require $\frac{a}{R^*} \ll 1^*$. Therefore to satisfy the condition of $\lambda \gg 1$, we require very large conductivity ratios of solid to fluid, $\frac{k_s}{k_f} \gg 1$. Alternatively this is satisfied by definition if the solids exist in vacuum.

Assuming that we satisfy the condition of isothermal solids, we address the conduction

between solids in their small regions of contact.

[more details]

4.2.1 Particle-particle conduction

Handling the heat transfer between contacting particles has been investigated extensively by researchers in a number of fields.[?,?,?,?,?,?] The amount of energy per time that can be transported per difference in temperature between pebble i and j as a conductance h_{ij}. Defined as

$$\frac{h_{ij}}{k^*} = 2\left[\frac{3F_n R^*}{4E^*}\right]^{1/3} \tag{4.7}$$

$k^* = 2k_i k_j/(k_i + k_j)$ is the effective solid conductivity of the two particles, and F_n is the magnitude of the normal force between particles i and j as calculated by Eq. ??. Therefore, if we consider particles at temperatures T_i and T_j in contact, they will transfer heat at a rate of

$$Q_{ij} = h_{ij}(T_i - T_j) \tag{4.8}$$

4.3 Nusselt number for spheres in packed beds

CHAPTER 5

Pebble Modeling: Discrete Element Method

This chapter presents the motivations and background of this study. First, it discusses energy usage in our society and the inevitable production of waste mechanical and thermal energies and their ubiquitous nature. This is followed by a brief discussion of common methods of converting ambient mechanical energy and waste heat into useful electrical energy. This chapter concludes with the objectives of this study and the scope of the document.

5.1 Background

In the framework of the discrete element method, we track particle motion in a Lagrangian sense. In the ensemble of particles, each particle's position, velocity, and acceleration are tracked and updated based on balances (or imbalances) of forces acting upon the particle. The discrete element method for granular material

5.1.1 Numerical Implementation Overview

The primary computational tools used in this study is LAMMPS (Large-scale Atomic/Molecular Massively Parallel Simulator);[?] a classical molecular dynamics code. The package of code, maintained by Sandia National Labs (http://lammps.sandia.gov), has many features making it particularly attractive for our use on the simulation of pebble beds. LAMMPS is open-source and written in highly-portable C++ allowing customization of any feature used in modeling. LAMMPS runs with distributed-memory message-passing parallelism (MPI) and provides simple control (manual or automatic) of the spatial-decomposition of simulation domain for parallelizing. The code can be built as a library so that LAMMPS can be coupled

to other code or wrapped with Python as an umbrella script. Perhaps most importantly, LAMMPS provides an efficient method for detecting and calculating pair-wise interaction forces; the largest consumer of run-time in the DEM algorithm.[?]

LAMMPS provides modeling of granular particle types; the use of LAMMPS for studying granular material since at least 2001 when Silbert, et al[?] studied granular flow on inclined planes. However, usefulness of LAMMPS for studying granular systems was greatly enhanced by LIGGGHTS (LAMMPS Improved for General Granular and Granular Heat Transfer Simulations), a suite of modules included on top of LAMMPS. LIGGGHTS has many academic and industrial contributors from around the world, with the code maintained as open-source by DCS Computing, GmbH.

Some notable features LIGGGHTS has added to LAMMPS include: Hertz/Hooke pair styles with shear history, mesh import for handling wall geometry, moving meshes, stress analysis of imported meshes, a macroscopic cohesion model, a heat transfer model, and improved dynamic load balancing of particles on processors.[?] Both LIGGGHTS and LAMMPS are distributed under the open-source codes under terms of the Gnu General Public License.

We will review some of the important physical modeling from LAMMPS/LIGGGHTS as they relate to features we wish to investigate for packed beds of pebbles in fusion reactors.

5.2   Particle dynamics

5.2.1   Particle interaction

If all the forces acting upon particle i are known, we simply integrate Newton's equations of motion for the translation degrees of freedom:

$$m_i \frac{\mathrm{d}^2 \mathbf{r}_i}{\mathrm{d}t^2} = m_i \mathbf{g} + \mathbf{f}_i \tag{5.1}$$

where m_i is the mass of this particle, $\mathbf{r}_i$ its location in space, g is gravity, and $\mathbf{f}_i$ represents the sum total of all external forces acting on this particle.

Two spherical particles, with radii R_i and R_j, interact when their overlap, δ, defined as:

$$\delta_{ij} = (R_i + R_j) - (\mathbf{r}_i - \mathbf{r}_j) \cdot \mathbf{n}_{ij} \tag{5.2}$$

is positive, with the unit vector $\mathbf{n}_{ij}$ pointing from particle j to i. Not coincidentally, the overlap is the same term as that defined in Hertz theory of § 2.1. When the two particles (or a particle and a boundary) are overlapping, the contact force between them can be calculated. Traditionally, the contact force is decomposed into a normal and tangential component,

$$\mathbf{f}_{ij} = \mathbf{f}_{ij}^n + \mathbf{f}_{ij}^t \tag{5.3}$$

Both the normal and tangential forces will employ a Maxwell material model to capture the viscoelastic properties of the solid. The Maxwell model is commonly represented as being a spring (purely elastic) and dashpot (purely viscous) connected in series. We will first address the normal contact.

5.2.2 Normal forces

The generic form of the normal force contact between two particles, i and j, when expressed in the simplest spring-dashpot model is

$$\mathbf{f}_{ij}^n = k_{ij}^n \delta_{ij} \mathbf{n}_{ij} - \gamma_{ij}^n \mathbf{u}_{ij}^n \tag{5.4}$$

where k_{ij}^n is the normal-direction spring coefficient, γ_{ij}^n is the normal-direction damping coefficient, and $\mathbf{u}_{ij}^n$ is the relative normal velocity between the two particles,

$$\mathbf{u}_{ij}^n = (-(\mathbf{u}_i - \mathbf{u}_j) \cdot \mathbf{n}_{ij})\mathbf{n}_{ij} \tag{5.5}$$

For the stiffness coefficient of normal contact for spherical pebbles used in solid breeder designs, it is appropriate to use the interaction dynamics defined by Hertzian contact laws, as given in § 2.1. Thus the non-linear spring constant is

$$k_{ij}^n = \frac{4}{3} E_{ij}^* \sqrt{R_{ij}^* \delta_{ij}} \tag{5.6}$$

The damping coefficient arises to account for the energy dissipated from the collision of two particles[?,?,?] is defined in this work as,

$$\gamma^n = \sqrt{5}\beta \sqrt{m^* k_{ij}^n} \tag{5.7}$$

with β as the damping ratio, and the pair mass, $m^* = \frac{m_i m_j}{m_i + m_j}$. For a stable system with $\beta < 1$, the damping ratio is related to the coefficient of restitution, e, in the following form

$$\beta = -\frac{\ln e}{\sqrt{\ln^2 e + \pi^2}} \tag{5.8}$$

5.2.3 Tangential forces

The tangential spring constant from Mindlin modification of Hertz theory, as given in § ??,

$$\mathbf{f}_{ij}^t = k_{ij}^t \delta_{ij}^t \mathbf{t}_{ij} - \gamma_{ij}^t \mathbf{u}_{ij}^t \tag{5.9}$$

where the fictive tangential overlap is truncated to so the tangential and normal forces obey Coulomb's Law,

$$\mathbf{f}_{ij}^t \leq \mu_i \mathbf{f}_{ij}^n \tag{5.10}$$

with μ as the coefficient of friction of the particle, i. The overlap is integrated from the tangential velocity over the time of contact.

$$\delta_{ij}^t = \int_{t_{c,0}}^t \mathbf{u}_{ij}^t \, \mathrm{d}\tau \tag{5.11}$$

The relative tangential velocity is found similar to the normal velocity,

$$\mathbf{u}_{ij}^t = (-(\mathbf{u}_i - \mathbf{u}_j) \cdot \mathbf{t}_{ij})\mathbf{t}_{ij} \tag{5.12}$$

The stiffness coefficient of tangential contact is

$$k_{ij}^t = 8G_{ij}^* \sqrt{R_{ij}^* \delta_{ij}^t} \tag{5.13}$$

where G_{ij}^* is the pair bulk modulus,

$$\frac{1}{G_{ij}^*} = \frac{2(2 + \nu_i)}{E_i} + \frac{2(2 + \nu_j)}{E_j} \tag{5.14}$$

The tangential dissipation coefficient is defined as

$$\gamma_t = 2\sqrt{\frac{5}{6}}\beta\sqrt{k_{ij}^t m^*} \tag{5.15}$$

It is worthwhile to point out one significant advantage of the format of the elastic and viscous coefficients, namely that they are determine completely from material and geometric properties: Young and bulk modulus, Poisson ratio, coefficient of restitution, density, and size (radius) of the particles in our system.

5.2.4 Integration

velocity-verlet

The force field defined by Eq. 5.1 is instead expressed in terms of the acceleration of the particle. The subscripts of i will be temporarily omitted from all of the per-particle quantities. Instead, time-varying quantities will have a subscript to refer to their timestep. Quantities at the current timestep will have subscript t, future timestep (either half step or full step) will have subscript $t + \Delta t$.

$$\mathbf{a}_t = \mathbf{g} + \frac{\mathbf{f}_t}{m} \tag{5.16}$$

The first step in the velocity-verlet algorithm is to integrate the position of the particle based on the current timestep's velocity and acceleration.

$$\mathbf{r}_{t+\Delta t} = \mathbf{r}_t + \mathbf{v}_t \Delta t + \frac{1}{2}\mathbf{a}_t \Delta t^2 \tag{5.17}$$

The particles at new positions interact as a function of their overlaps (see Eqs. **??**). Acceleration at the next timestep is then calculated again from the updated forces in Eq. 5.16. As a last step, the velocity at the next timestep is found from an average of the two accelerations,

$$\mathbf{v}_{t+\Delta t} = \mathbf{v}_t + \frac{\mathbf{a}_t + \mathbf{a}_{t+\Delta t}}{2}\Delta t \tag{5.18}$$

5.3 Granular heat transfer

Much like our treatment of the momentum of every particle in DEM, we handle the energy in the Lagrangian specification. The temperature of particle i, for example, is found from the first law of thermodynamics

$$\rho_i V_i C_i \frac{\mathrm{d}T_i}{\mathrm{d}t} = Q_{s,i} + Q_i \tag{5.19}$$

where ρ, V, and C are the density, volume, and the specific heat of the solid, respectively.

On the right hand side of Eq. 5.19, is the nuclear heating source term, Q_s, and the total heat transferred to/from particle i via conduction to neighboring particles,

$$Q_i = \sum_i^Z Q_{ij} \tag{5.20}$$

The conductive heat transfer to neighboring particles was discussed in length in § **??**. In that section we derived Eq. 4.7 as a conductance term between neighboring particles. It is repeated here for reference:

$$\frac{h_{ij}}{k^*} = 2 \left[\frac{3F_n R^*}{4E^*} \right]^{1/3}$$

where the * terms are the effective properties of the two particles under consideration. Therefore, if we consider particles at temperatures T_i and T_j in contact, they will transfer heat at a rate of

$$Q_{ij} = h_{ij}(T_i - T_j) \tag{5.21}$$

We are assuming that in a single timestep a pebble is transfering heat only with its immediate neighbors. Vargas and McCarthy[?] provide arguments for the validity of Eq. ?? given numeric time steps and contact areas. The conclusion is that any time step that satisfies stability of the particle dynamics will automatically satisfy particle heat transfer.

5.3.1 Thermal expansion

Owing to the impact thermal expansion has on pebble bed structures undergoing thermal cycling,[?,?,?] we also included a simple thermal expansion model. The diameter of the pebbles was updated after a specific number of timesteps according to the following

$$d_i = d_{0,i} \left[1 + \alpha \left(T_i - T_{\text{ref}} \right) \right] \tag{5.22}$$

where α is the thermal expansion coefficient, T_i is the temperature of the pebble at the current step, and $d_{0,i}$ is the diameter of the pebble at temperature T_{ref}.

5.3.2 Pebble Bed Heat Transfer: Test Case

In our pebble bed test case, we establish heat transfer that is essentially one-dimensional in the x-direction. The pebble bed has very little variation of forces and temperatures in the y-direction due to the periodic boundary condition at the edges of the domain. Gravity effects are minor in the overall heat transfer and induce only a slight z-dependency to the

results. With the one-dimensional assumption, we step back into a continuum mechanics formulation to aid us in finding an effective thermal conductivity of our numeric pebble bed.

A steady state for a material with constant temperature boundary conditions ($T(\pm 10d) = T_s$) and nuclear heating has the following heat equation

$$0 = \frac{\mathrm{d}^2 T}{\mathrm{d}x^2} + \frac{q'''}{k_{\mathrm{eff}}} \tag{5.23}$$

In this continuum mechanics formulation, we are assuming that the nuclear source, q''' term is applied evenly over the entire volume. In our DEM formulation, our source term applies to a single pebble. To find the effective thermal conductivity of our pebble bed, we must reconcile this discrepency. This is accomplished with the exchange of

$$q''' = \frac{Q_{\mathrm{tot}}}{V_{\mathrm{tot}}} = \frac{Q_s N}{300 H d^2} \tag{5.24}$$

where H is the average height of the top layer of pebbles. We apply symmetry about the centerline and impose our boundary conditions to solve the differential equation. If we take the temperature of the midplane as $T(0) = T_0$, we back-out an effective thermal conductivity (ETC) as

$$k_{\mathrm{eff}} = \frac{Q_s N}{6 H (T_0 - T_s)} \tag{5.25}$$

We will use this formulation to analyze and compare our test-case pebble beds.

5.4   Stability study

The velocity-Verlet algorithm is an efficient means of updating the kinematics of all the particles in the ensemble. However, when applied to the models of ceramic breeder pebbles, there are unique issues that we must address. On the one hand, like all explicit, time-dependent finite difference schemes, we must be careful to avoid instabilities and this tends to require very small timesteps. On the other hand, the thermal time-constants in the

ceramic breeder zones can be many hundreds of seconds. These two conditions can lead to unacceptably large requirements on the number of timesteps for a thermal DEM simulation.

In this section we will demonstrate the calculation of approximate stable DEM timesteps as a function of material properties of ceramic pebbles. Then with that knowledge in hand, we will argue for scaling certain physical properties to allow for faster simulations without sacrificing fidelity to the real physics of the problem.

5.4.1 Critical timestep

When a force is applied to the surface of an elastic body, the force propagates along the surface at the wave speed first solved by John William Strutt, 3rd Baron Rayleigh[?] (when he wasn't discovering the scattering phenomenon explaining why the sky is blue or winning the Nobel prize for discovering Argon),

$$u_{\mathrm{Ra}} = \alpha \sqrt{\frac{G}{\rho}} \tag{5.26}$$

where, again, G is the shear modulus and ρ is the density of the elastic material. The α coefficient is a complicated function coming from Rayleigh's solution but can be approximated as[?]

$$\alpha = 0.1631\nu + 0.876605 \tag{5.27}$$

for realistic values of Poisson's ratio of elastic materials. From the inverse of the Rayleigh wave frequency, we can directly find a timestep for Rayleigh waves,

$$\delta t_{\mathrm{Ra}} = \frac{\pi R}{u_{\mathrm{Ra}}} \tag{5.28}$$

When we write this for any particle, i in the ensemble (exchanging the shear for elastic modulus),

$$(\delta t_{\text{Ra}})_i = \frac{\pi R_i}{0.1631\nu_i + 0.876605} \sqrt{\frac{2(1 + \nu_i)\rho_i}{E_i}} \tag{5.29}$$

We allow for the particles in the system to have varying density, elastic modulus, and size. Therefore the critical timestep for the entire systme is governed by the minimum value of any particle's Rayleigh timestep.

$$\delta t_c = \min_{\forall i} \left[(\delta t_{\text{Ra}})_i \right] \tag{5.30}$$

The ceramic materials identified for breeders have relatively high Young's moduli, on the order of 10^{10}Pa. The smallest radius will be on the order of 10^{-4}m. The ceramic density is approximately on the scale of 10^4kg/m^3. Finally, to prevent pebbles from cracking in the ensemble, it is reasonable to assume that the maximum contact forces will on the order of 10^2N. These values lead to a necessary timestep of

$$\delta t_c \propto 10^{-7}\text{s} \tag{5.31}$$

For a simulation that may last several hundreds of seconds of real time, this then requires more than 10^9 timesteps. If we have 10^4 particles in the simulation, each having their position integrated over a billion times, it becomes obvious that computational time is a major issue for our simulations of nuclear heating of ceramic breeder pebbles. If we are able to reduce the critical timestep (while perhaps decreasing the simulation time), the simulations will be much more practical for use.

5.4.2 Simulation acceleration with scaled material properties

I wish to rewrite Eq. 5.29 to facilitate a discussion on the parameters. Isolating each material term gives,

$$\delta t_c \propto R_i \times \frac{\sqrt{2(1 + \nu_i)}}{0.1631\nu_i + 0.876605} \times \rho_i^{1/2} \times E_i^{-1/2} \tag{5.32}$$

[pretty sure the approximation for ν only works when it's less than 1 so can't scale. must find out for sure.]

The most direct effect would come from scaling the radius

5.5 Pebble failure modeling

The discrete element method has been used for studies in a variety of fields for studying inter-particle forces and the homogeneously distributed force networks that arise in packed beds (for example, see Ref.[?]). The discrete element method was also used in the fusion community to attempt to model failure initiation and propagation.[?,?,?] They too observed that a relatively few number of high-force networks, distributed troughought the bed supported the external mechanical loads. The even distribution of the force networks was used to defend the development of a probability-based predictor for failure. We make use of the probability argument of Zhao, et al. for the current study.[?] Their basic premise is that probability distributions of strength curves for pebble crushing have been observed (see, for example crush loads of Ref.[?]). Then in DEM models, a probability distribution of inter-particle forces are also observed. Overlaying the two probabilities resulted in seemingly random locations of pebbles satisfying the failure criteria – not strictly along the high-force chains running through packed beds.

We apply the theory of Zhao, et al. in the following manner. If pebbles fail at random locations, we may de-couple the task of predicting pebble failure (i.e. finding the mechanical or thermal load that causes a pebble to fail) from the task of modeling the ramifications of pebble failure. In our model, we begin with a starting point of a packed bed and then simply flag pebbles at random for 'failing'. For our first model of failure, after a pebble has been flagged it is removed from the system entirely. The removal disrupts the meta-static state of the ensemble and the remaining pebbles re-settle. In reality, the ceramic pebbles generally break into just a few large pieces that remain in the system. Under development is a method for recreating that behavior in the DEM domain, it will be reported in future studies.

Table 5.1: Maximum load and nominal tension.

E (GPa)	ν	k (W/m-K)	C (J/kg-K)	α (1/K)
126	0.24	2.5	1156	15×10^{-6}

Our three-dimensional system consists of mono-dispersed particles of diameter d. The particles are constrained by two rigid walls in the x-direction at locations of $x = \pm 10d$ and periodic boundary conditions in the y-direction located at $y = \pm 7.5d$. Gravity acts in the downward z-direction and the particles are bound from below by a rigid wall at $z = 0$. The size of the system allows approximately 10 000 particles to fill to a height of approximately $z = 30d$. The volume was chosen to represent the long, tall, narrow channels seen in many solid breeder module designs.[?,?,?]

5.5.1 Material properties

For this study, the material was chosen as lithium metatinatate with all properties coming from Ref.;[?] they are summarized in Table 5.1

5.5.2 Methodology

All the test cases begin with a common starting point of a filled, lightly packed volume of 10 550 pebbles. The pebbles are poured into the volume from above and come to rest under the influence of gravity (see Fig. 5.1). Initially, to recreate how we may pack solid breeders in reality, we attempted vibration simulations in order to pack the pebbles into a more dense state. However, we found the same packing states (from a void fraction standpoint) could be realized in a more computationally-simple manner by lowering a z-plane wall onto the top of the packed bed until it experienced some small force. This pour-press-packing routine was repeated many times and all the beds exhibited the same force on the top wall at roughly the same packing fraction. We took the last case, with a packing fraction (volume of N pebbles
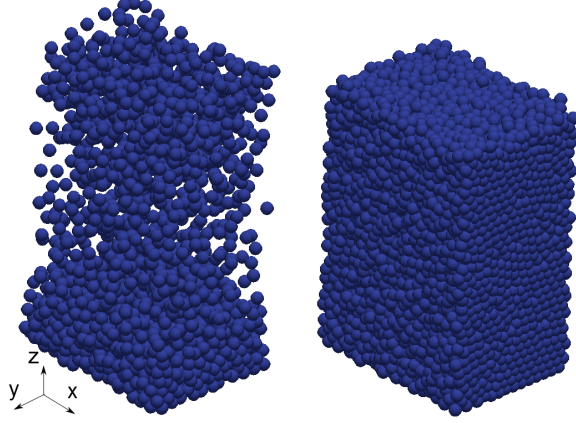
Figure 5.1: Demonstrating the pouring process of $N = 10\ 550$ pebbles into the control volume with an early (left) and late (right) snapshot.

per total volume) of $\phi_{\text{bl}} = 62.9\%$, as our baseline configuration. The packed bed state was saved and used as a starting point for numerous 'failed' cases to be described later.

For the baseline case, we assigned an initial temperature of T_{ref} to both the pebbles and the x walls, then set a constant nuclear heating source on each pebble. The nuclear energy raised the temperature of the pebbles while the walls remained at T_{ref} for cooling. The process ran until a steady state was reached (for example, see Fig. 5.2); the total thermal energy of the bed, $E = \sum_i^N m_i C_i T_i$, was monitored and the simulation completed when the value was constant. At steady state, we analyzed thermomechanical characteristics of the pebble bed such as effective thermal conductivity, average coordination number, temperature profiles in the bed, and inter-particle contact forces.

As mentioned in Sec. 5.5, in this study we model pebble failure without considering the cause of failure. This is done by randomly selecting pebbles from the ensemble, regardless of forces acting upon the pebble, and removing them entirely. When a pebble is removed, the neighboring pebbles react due to the imbalance of forces and the bed settles into a new configuration. We differentiated the failed beds by their percentage of failed pebbles: η = number of failed pebbles per original ensemble size. After failing we again applied our heating routine.
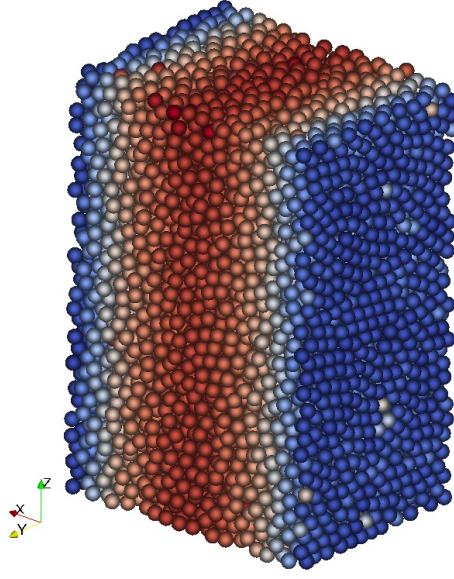
Figure 5.2: Temperature distribution of pebbles in the 10% failed bed. At the end of steady-state heating, a one-dimensional profile is evident in all pebble beds studied here. The pebbles are receiving nuclear heating. Cooling proceeds through the pebbles in contact with the walls in the x-direction. [color online]

5.6   DEM solver

Time-discretization of the integration of Eq. 5.1 is handled by the core Large-scale Atomic/Molecular Massively Parallel Simulator (LAMMPS) code released by Sandia National Laboratories.[?,?] The code calculates velocity and position via the semi-explicit velocity-Verlet integration. The algorithm is stable with a global error of approximately $O(\Delta t^2)$ for displacement; details can be found in Ref.[?]

In the process of the study, to demonstrate the ability of the dynamic integration to capture resettling (and any possibly asymmetries), some beds were generated wherein the failure of pebbles was slightly localized near one or both x-walls. The profile of the pebbles near the top of the stack, after resettling, are shown in Fig. 5.3.

In our work, we occasionally required a fully quiesced bed. To determine when this occurred, the total kinetic energy of the entire ensemble was monitored and a packed bed was considered to have completely settled once the kinetic energy of the system was less

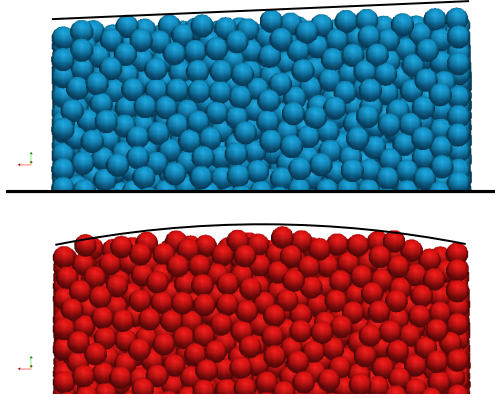Figure 5.3: Demonstrating the dynamic resettling from an example study done on location bias to pebble failure. The top image had the pebbles near the left wall biased to fail. The bottom image had a bias for the pebbles near both walls to fail. The lines are drawn as an aid to the eye.

than 10^{-9}; similar to the process described in Ref.[?]

The granular heat transfer equations (Eqs. **??-??**) are layered onto the LAMMPS code via a package of code named LIGGGHTS (LAMMPS Improved for General Granular and Granular Heat Transfer Simulations[?]). Parallelization of the code is straightforward with LAMMPS and we run the code on 128 nodes of UCLA's Hoffman2 cluster for typical run times of 18 to 24 hours per routine (e.g. filling, packing, heating, etc.).

5.7   Results and discussions

The aim of this study was both to discover the impact of pebble failure on thermomechanical properties as well as determine the impact as a function of the number of failed pebbles. To satisfy the latter, we created beds with $\eta = 1\%$, 5%, 10%, and 15% of pebbles failed.

We first compare steady-state temperature profiles in the test beds against the one-dimensional theory of Eq.**??**. To find the temperature profile in x, we create volumes of width Δx that extend through the limits of the y- and z-directions. We then find the n pebbles residing in the slices and take the mean value of their temperatures, $\langle T \rangle = \sum_i^n T_i/n$

of all pebble temperatures that have coordinates inside the slice. Below we will omit the notation $\langle T \rangle$ with the understanding that temperatures are volume-averages. Using the volume slices, we also find the average coordination number, $\langle Z \rangle = \sum_i^n Z_i/n$, normalized average contact force, $\langle F^* \rangle = [\langle F \rangle / \langle F_{bl} \rangle_{\max}]^{1/3}$, and the normalized average temperature difference between pebbles in the slice, $\langle \Delta T_{ij} \rangle / (T_0 - T_s)_{\mathrm{bl}}$; parameters which are discussed later.

When analytically solving Eq. **??**, we introduce non-dimensional temperature, $\theta_{1\mathrm{D}} = (T - T_s)/(T_0 - T_s)$, and spatial, $x^* = x/L$, variables and the solution becomes purely geometric; $\theta_{1\mathrm{D}} = 1 - x^{*2}$. We plot this theoretical solution against the temperature profiles coming from the steady-state DEM simulation in Fig. 5.4. We find that all our models had a nearly perfect match to a one-dimensional prediction, validating the calculation of effective thermal conductivity in this study.

Another concern we had for pebble failure, was the phenomenon of 'jamming' during resettling that would possibly leave pebbles isolated from their neighbors (apart from those they are resting upon). Such an isolated pebble would have no strong pathway for heat transfer and heat up much higher than that of its neighbors. Evidence of pebble isolation and 'hot-spots' would be apparent in Fig. 5.4 as localized deviations of data points from the quadratic profile. However, no deviations are seen in the data and we conclude that hot-spots will not be a concern in a packed bed.

The effective thermal conductivity is found for all of our pebble beds, via Eq. 5.25, then normalized against the conductivity of the baseline ensemble ($k_{\mathrm{eff}}^* = k_{\mathrm{failed}}/k_{\mathrm{bl}}$). Figure 5.5 shows the decreasing ETC with pebble failure. When 15% of the pebbles are crushed in a pebble bed, the ETC has fallen all the way to only $k_{\mathrm{eff}}^* = 0.30$. This large reduction is especially important in light of the already poor thermal management of virgin pebble beds that, even in helium environments, have been experimentally measured at only approximately 1 W/m-K (see, e.g., Refs.[?,?]). In well-packed pebble beds, the ETC is generally related to the packing fraction. In Fig. 5.5, this relationship seems weak as the effective conductivity drops much more rapidly than does the packing fraction as the number of broken pebbles in
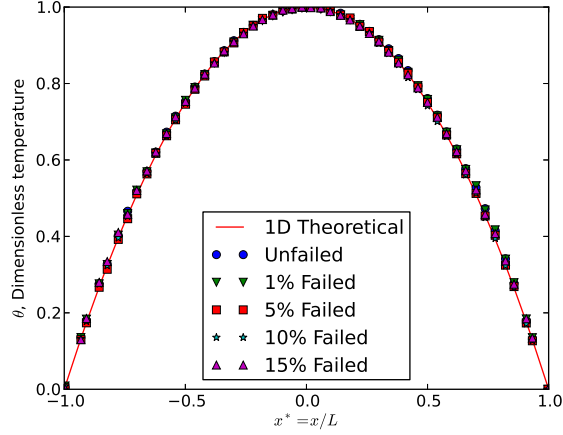
Figure 5.4: The non-dimensional temperature profiles for each test case follow the theoretical shape of a one-dimensional, constant k, continuum solution.

the ensemble increases. To find the cause of decrease in conductivity and to make use of the information provided by DEM tools, we look to other parameters than the packing fraction.

From Eq. **??**, in the steady-state, the energy input by nuclear heating must be balanced by the transport of heat out of a pebble into its neighbors. Inter-particle heat transfer is dictated by the number of neighboring contacts, temperature difference between pebbles, and the thermal conductance, h_{ij} through the contact area. The thermal conductance is, itself, a function of material properties (which are essentially constant here) and the force at the contact, going as $h_{ij} \propto F_n^{1/3}$. Thus, the net heat out is a function of the three variables as

$$Q_{\mathrm{net}} = f(Z, F_n^{1/3}, \Delta T) \tag{5.33}$$

The variables affecting Q_{net} are plotted in Fig. 5.6. The average coordination number, shown in the bottom plot, decreases from a mid-line value of about 7.0 at the steady-state of the baseline case down to a mid-line value of 5.5 for the 15% failed bed; a reduction of about 80%. But this number doesn't compare with the large reduction in ETC which was $k_{\mathrm{eff}}^* = 0.30$. Clearly, there are fewer contacts in the pebble bed after failure but this alone does not account for the reduction in ETC.
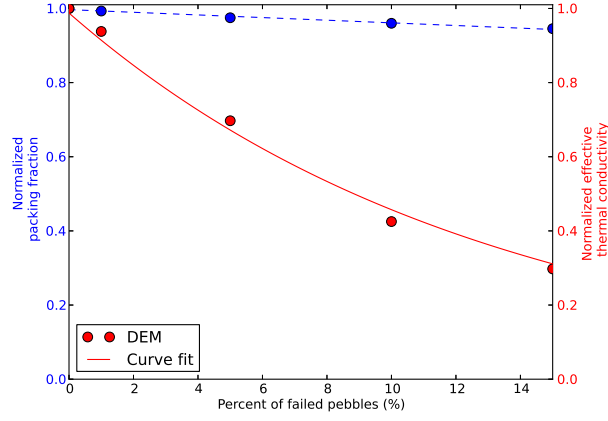
Figure 5.5: The normalized effective thermal conductivity (solid line) follows an exponential decay relationship with amount of failed pebbles. The normalized packing fraction (dashed line), compared to thermal conductivity, is relatively constant and is more closely fit to a linear reduction.

Much more dramatic, seen in the center plot, is the reduction in average normal force seen by pebbles after many of the neighbors fail and are removed from the system. From the baseline down to the 15% failed case, the contact forces are dramatically reduced to about $\langle F^* \rangle = 0.1$. This reduction in force is joined by an increase in average neighbor temperatures which are 3 times higher for the bed with most failed pebbles when compared to the baseline.

The results shown in Fig. 5.6 demonstrate that the heat transfer through a pebble bed is simultaneously a function of the coordination number and inter-particle contact forces – which are both reduced as pebbles in the bed fail – as well as the temperature difference between pebbles at steady state – which increases as pebbles in the ensemble fail. Interestingly, when a pebble bed has lower overall inter-particle contact forces fewer particles would be expected to break. This would imply that pebble breakage is self-dampening; as pebbles begin to break the ensemble quickly relaxes and avoids future pebble failure. So while we induced failure up to $\eta = 15\%$, such large values may not occur in real beds.

Another feature of Fig. 5.6 worth noting is the increase in averaged normal contact forces near the center of the bed relative to the walls. In the assumptions used to develop this

34
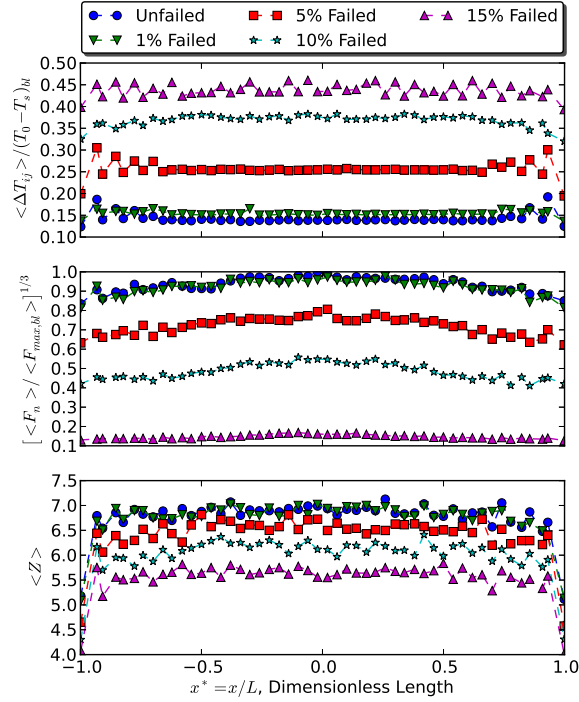
Figure 5.6: Average temperature differences between neighboring pebbles (top), contact forces (middle) and coordination numbers (bottom). The profiles of average coordination number and contact forces in the bed decrease in value with increasing pebble failure. Fewer and weaker contacts will reduce the possible paths of heat transfer from a pebble and this results in higher average temperatures between neighbors.

simulation, we had noted the lack of localized force concentrations in a bed under an external mechanical load. However, in these results, owing to the nuclear heating temperature profile and thermal expansion of each pebble, there is a bias toward higher forces in the center of the bed. This result highlights the need for a model to predict failure initiation in place of the assumption of random pebble failure.

5.8   Conclusions

The current study aimed at properly simulating a pebble bed with a specified fraction of the pebbles failing during operation; then determining the repercussions of the failures as they

affect the macroscopic property of effective thermal conductivity. We used the assumption of homogeneous, random locations of pebble failure to induce a failure routine without requiring external loads on the bed to permit beds that could be directly compared. After heating to a steady-state, an effective thermal conductivity was calculated for the pebble bed. The results show that small amounts of pebble failure correspond to large decreases in the conductive transport of energy through the pebble bed. The increase was due primarily to a drop in the inter-particle forces which lead to a large increase in temperature differences between neighboring pebbles. We note again, however, that this value has been calculated in the absence of interstitial gas so the results apply only to the reduction in energy transferred via inter-particle conduction.

The assumption of homogeneous distribution of pebble failure was found to be inappropriate after a pebble bed reached steady state nuclear heating. The scheme assumes no localization of average forces in the bed but we found an average force profile that had a maximum at the center and minimum at the walls. The next step of modeling will eliminate the error of such an assumption as we must combine failure prediction to failure outcome modeling.

CHAPTER 6

Modeling CFD-DEM

[talk about how lacking the DEM result is without the inclusion of helium in analysis. There are some Fusion papers on conductivity in vacuum and with helium]

We now consider the influence of helium on thermal transport of deposited nuclear energy as it is carried away by the cooled structural walls. We begin by considering the fluid in a continuum sense and the pebbles in a discrete one. The interactions of the fluid and solid are characterized by effective relationships in each discretized cell of fluid. We then consider an mesoscopic approach to the fluid-solid interaction with the Lattice-Boltzmann method.

The chapter begins with introduction of the coupled fluid dynamics - discrete element method (CFD-DEM) approach: governing equations, discretization techniques, and algorithms.

We then do LBM. And stuff.

6.1   Numerical Methodology

Models based on the discrete element method (DEM) are currently the only tools available that can extract information on individual pebble interactions. The DEM formulation provides information such as inter-particle forces and individual particle temperatures, which are necessary for predicting and simulating morphological changes in the bed (e.g. pebble cracking, sintering, etc.) However DEM alone is not able to capture the effects, neither on momentum nor energy, of an interstitial fluid. Therefore we present two fluid modeling techniques to supplement the DEM computations. We will first discuss the fully dynamic coupling of the DEM model with a volume-averaged thermofluid model of helium. Then we

will introduce the integration of our DEM packing structure into lattice-Boltzmann simulations of the entire bed-fluid system.

6.1.1 DEM

The discrete element framework introduced in § 5.2 is augmented with a drag force term to capture interaction with surrounding fluid velocity fields. To accomplish this, we simply include a drag force to the Newtonian balance of forces given in Eq. 5.1. The momentum balance now reads:

$$m_i \frac{\mathrm{d}^2 \mathbf{r}_i}{\mathrm{d}t^2} = m_i \mathbf{g} + \mathbf{f}_i + \beta_i V_i \Delta u_{if} \tag{6.1}$$

where $\Delta u_{if} = u_f - u_i$, is the relative velocity between the fluid and pebble, i, and the inter-phase momentum exchange coefficient, β_i, acts upon the pebble volume (not to be confused with the damping coefficient introduced in § 5.2). Similarly, the energy equation now includes

$$m_i C_i \frac{\mathrm{d}^2 T_i}{\mathrm{d}t^2} = Q_{n,i} + \sum_{j=1}^{Z} Q_{ij} + \beta_{E,I} A_i \Delta T_{if} \tag{6.2}$$

where $\Delta T_{if} = T_f - T_i$, is the relative temperature between teh fluid and pebble, i, and the inter-phase energy exchange coefficient, $\beta_{E,i}$, acts upon the pebble surface area, A_i.

The trajectory of pebble i is updated based on the force terms on the right hand side of Eq. **??**: gravity, contact forces between particles (or particle-wall), and a drag force. Similarly, the temperature of the particle updates with the terms from Eq. 6.2: nuclear heating rate, inter-particle conduction, and now a heat transfer with surrounding fluid.

Drag forces from fluid flows through packed beds are found from volume-averaged, empirical correlations of either numerical or experimental studies. Considering a small region of a packed bed surrounding our particle of interest, i, the non-dimensional drag force is found only as a function of the local packing fraction of that region. In the zero Reynolds

38

number limit, the non-dimensional drag force reduces to a Stokes flow correlation that is only a function of the local packing fraction value, ϕ. For the value of particle Reynolds numbers seen by the helium purge gas, this is the dominant term. However, for a complete discussion of the non-dimensional drag terms see Refs. 5, 6. The correlation used in this study comes from the results of numerical studies of packed beds by Koch and Hill.[?,?,?] To arrive at their relationships, they did many lattice-Boltzmann simulations of porous flow.

$$\beta_i = \frac{18\nu_f\rho_f}{d_i^2}(1-\phi)F \tag{6.3}$$

where

$$F = \epsilon(F_0 + \frac{1}{2}F_3\mathrm{Re}_{p,i}) \tag{6.4}$$

Stokes flow

$$F_0 = \begin{cases} \frac{1+3\sqrt{\phi/2}+(135/64)\phi\ln(\phi)+17.14\phi}{1+0.681\phi-8.48\phi^2+8.16\phi^3} & \text{if } \phi < 0.4 \\ 10\frac{\phi}{(1-\phi)^3} & \phi > 0.4 \end{cases} \tag{6.5}$$

and high Reynolds contribution

$$F_3 = 0.0673 + 0.212\phi + \frac{0.0232}{(1-\phi)^5} \tag{6.6}$$

The packing fraction and void fraction in any fluid cell is calculated by summing through all the volumes of k particles located in that cell (or the complement thereof)

$$\phi = \sum_{i=1}^{k} \frac{V_{p,i}}{\Delta V_f} \tag{6.7}$$

Other forces, such as Magnus forces, are inconsequential on predominantly stationary packed beds and are not considered.

The inter-phase energy transfer coefficient is of the same form as a traditional heat transfer coefficient and is calculated from the Nusselt number for the helium flow (with conductivity k_f) through a packed bed.

$$\beta_{E,i} = \frac{\mathrm{Nu}_i k_f}{d_i} \qquad (6.8)$$

Li and Mason[?] summarize correlations for Nusselt number as a function of Reynolds number for packed beds with the following equations

$$\mathrm{Nu} = \begin{cases} 2 + 0.6(1-\phi)^n \mathrm{Re}_p^{1/2} \mathrm{Pr}^{1/3} & \mathrm{Re}_p < 200 \\ 2 + 0.5(1-\phi)^n \mathrm{Re}_p^{1/2} \mathrm{Pr}^{1/3} + 0.2(1-\phi)^n \mathrm{Re}_p^{4/5} \mathrm{Pr}^{1/3} & 200 < \mathrm{Re}_p \leq 1500 \\ 2 + 0.000045(1-\phi)^n \mathrm{Re}_p^{9/5} & \mathrm{Re}_p > 1500 \end{cases}$$

where $n = 3.5$ was found to fit best for small particles in dilute flows. [we should find a new value for high packing fraction]

Thus we have a formulation whereby a known fluid flow field and temperature throughout the domain, we can calculate the influence of that fluid on every particle's position and temperature. Next we will cover how we can calculate the flow field based on a volume-averaged influence of particles on the fluid.

6.1.2 Volume-averaged CFD Helium

The technique of coupling CFD to DEM was first proposed by Tsuji, et al9. In this formulation of the helium flow, a fluid cell is much larger than the individual particles (in application, this meant approx. 5 6 particles per cell) and as such, the particles themselves are not resolved in the fluid space but are simply introduced via volume-averaged terms. Therefore momentum and energy of a fluid flow through a solid phase is governed by volume-averaged Navier-Stokes and energy equations10. These equations are applied to a discretized volume of fluid space. For fluid cell, k, these are5:

$$\frac{\partial \epsilon_k \rho_f}{\partial t} + \nabla \cdot (\epsilon_k u_f \rho_f) = 0 \tag{6.9}$$

$$\frac{\partial \epsilon_k u_f}{\partial t} + \nabla \cdot (\epsilon_k u_f u_f) = -\frac{\epsilon_k}{\rho_f} \nabla P_f + \nabla \cdot (\nu_f \epsilon_k \nabla u_f) - \frac{S_k}{\rho_f} \tag{6.10}$$

$$\frac{\partial \epsilon_k T_f}{\partial t} + \nabla \cdot (\epsilon_k u_f T_f) = \nabla (\epsilon_k \epsilon \nabla T_f) - \frac{E_k}{\rho_f C_f} \tag{6.11}$$

where the fluid void fraction is the complement of the solid packing fraction, $\epsilon = 1 - \phi$. The momentum and energy exchanges with the solid phase are represented in the source terms. They are volume-weighted sums of the drag forces and energy exchanges, respectively, for all particles in the discretized fluid cell:

$$S_k = \frac{1}{V_k} \sum_{\forall i \in k} \beta_i V_i \Delta u_{if} \tag{6.12}$$

$$E_k = \frac{1}{V_k} \sum_{\forall i \in k} \beta_{E,i} A_i \Delta T_{if} \tag{6.13}$$

The inter-phase momentum and energy exchange coefficients act as the communicators between the particle information from the DEM solver and the fluid fields from CFD. Thus the motion and energy of the fluid field are intimately coupled with the particle positions and energy, but computational time is preserved by only considering volume-averaged values in the fluid domain. The cross-communication between fluid and solid is accomplished with a coupling routine that is explained in detail in Refs. 11, 12.

6.1.3 Modeling Setup and Procedure

The pebble bed has dimensions in the x-y directions of 20d×15d, respectively. There are structural walls, providing cooling, at the x-limits and periodic walls in the y-limits. 10 000 pebbles were loaded into the system which went to a height of approximately 24d after the bed was vibration packed. The pebble bed had a roof loaded at the upper limit of the z-direction that was lowered by force-control up to 6 MPa. This bed is referred to as the

'well-packed' bed. This was meant to simulate a fresh, densely-packed bed that is under compressive load during fusion operation. As such, this would be when pebbles would be likely to crack during operation. Therefore, based on the well-packed bed, a second bed was generated by simulating crushed pebbles; crudely the extensive crushing is simulated by simply removing 10% of the pebbles at random from the ensemble and then allowing the bed to resettle, from the now-imbalanced gravity and inter-particle forces, to a new stable packing structure. This bed is then referred to as the 'resettled' bed for the rest of the analysis. The intent is to deduce changes in thermomechanical properties from an ideally packed bed to one where significant cracking has altered the ideal morphology of the bed.
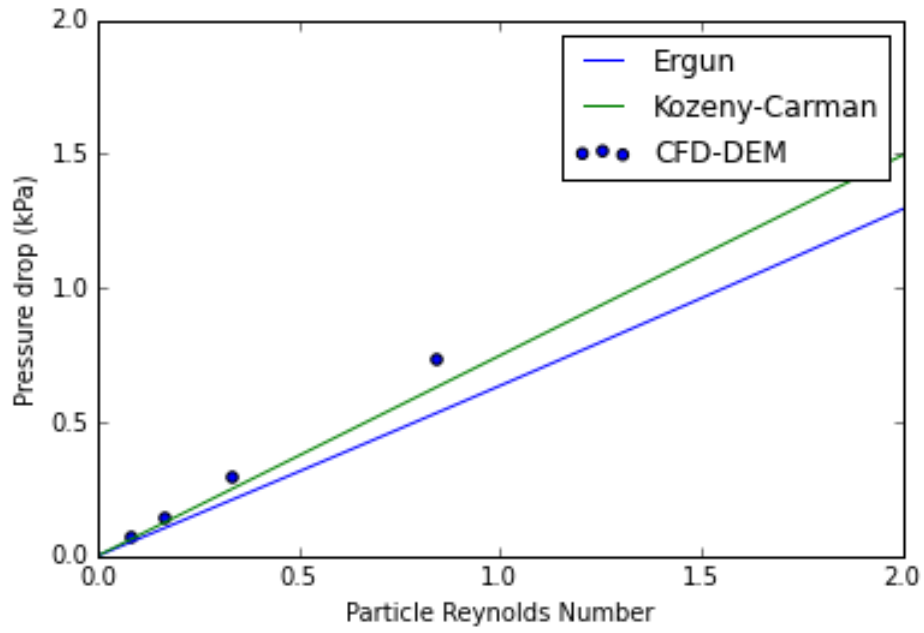
6.1.4 Pressure Drop

Before analyzing thermal results from the CFD-DEM coupling, the system was run at various particle Reynolds numbers and the overall pressure drop of the packed bed was measured. This value was compared against the well-known Kozeny-Carman and Ergun equations. The Kozeny-Carman is known to fit better with experimental data at very small Reynolds numbers. In Fig. 1 we see the CFD-DEM coupling model is providing bed-scale pressure drops that match very well with Kozeny-Carman over the Reynold's numbers applicable to helium purge flow in fusion reactors. The flow is visualized in Fig. 2. The pebble bed is clipped at the centerline to allow viewing of the helium streamlines. Apparent in the figure is temperature profiles in the helium from centerline to wall that qualitatively mirror temperature profiles in the pebble bed.

6.1.5 Effective thermal conductivity from CFD-DEM

The well-packed and resettled pebble beds were run to thermal steady-state with nuclear heating and wall cooling in both pure DEM and coupled CFD-DEM simulations for comparison. From steady-state temperature distributions, seen in the pebble scatter plots in Fig. 3, an average profile is calculated and an effective thermal conductivity computed. The
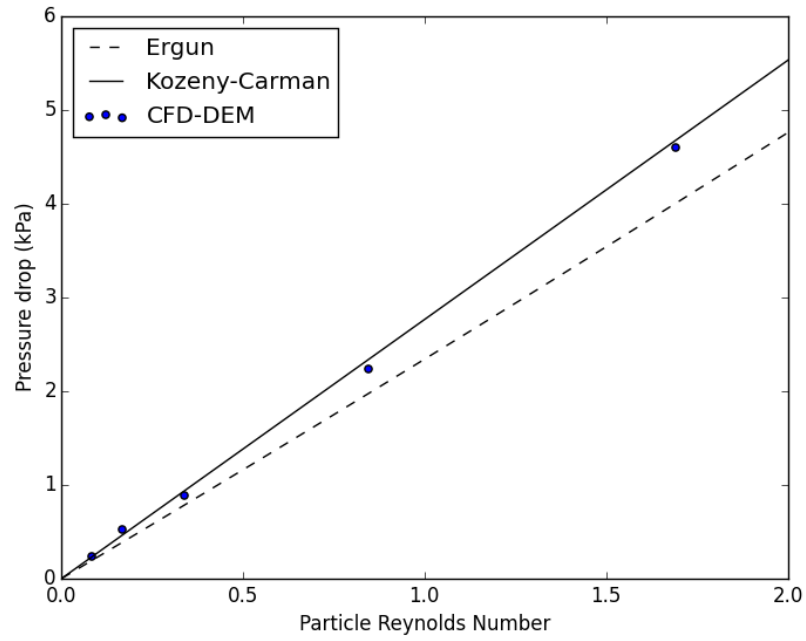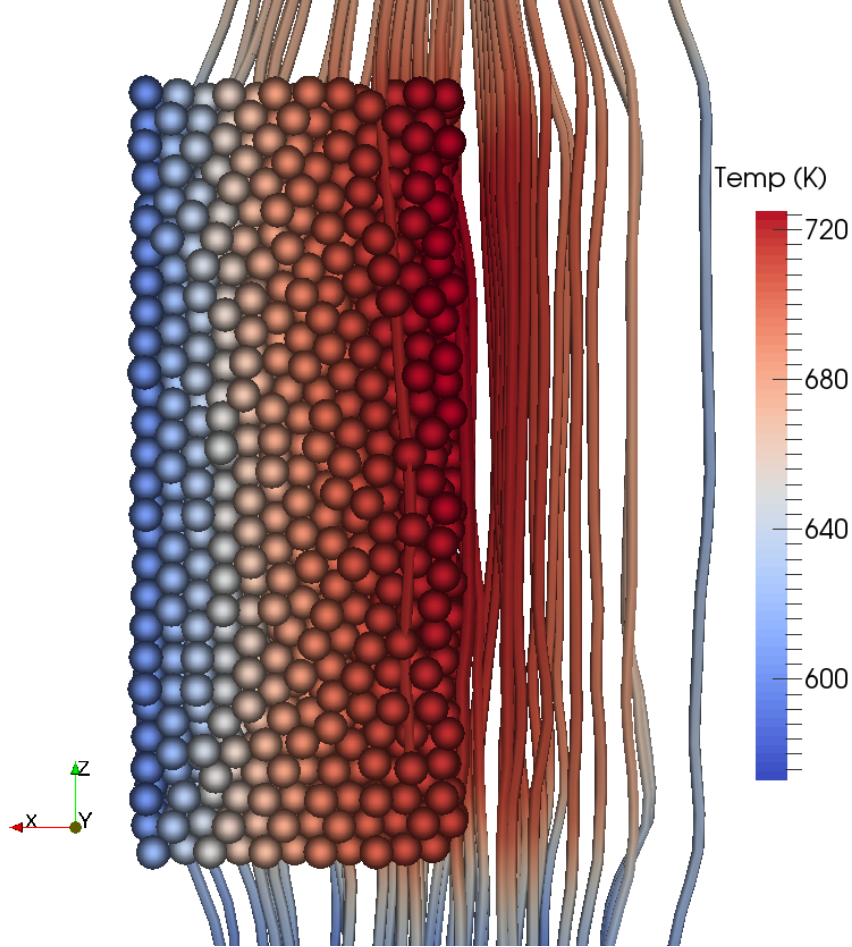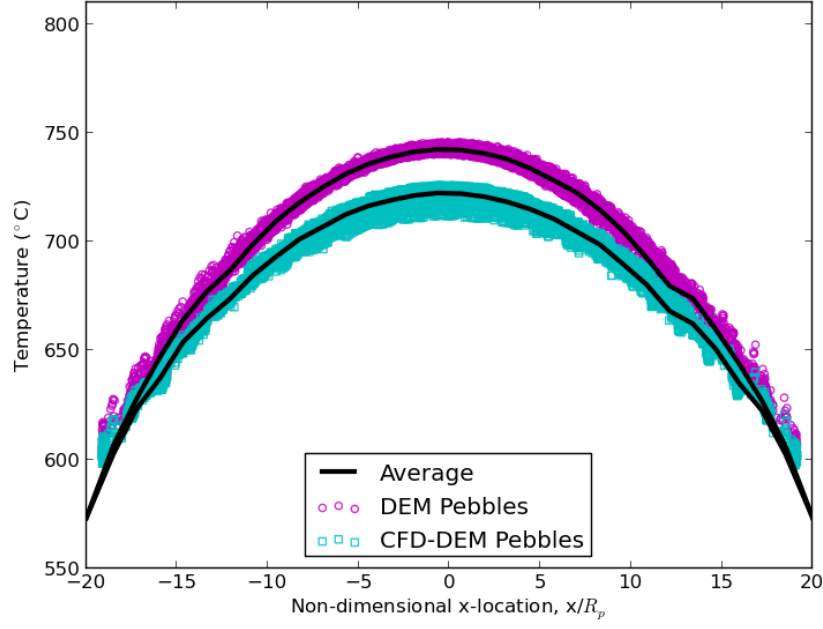
(a) Well-packed bed

(b) Re-settled bed

Figure 6.1: Pressure drop calculations across packed beds, solved by CFD-DEM, fit well to the Kozeny-Carman empirical relation.

Figure 6.2: Cut-away view of the pebble bed with streamlines of helium moving in generally straight paths from inlet to exit.

values are tabulated in Table I. In the case of pure DEM, energy is transported solely along conduction routes in the ensemble. When the packing of the bed is disturbed, this results in a substantial drop in effective conductivity (a drop of 31%). The details of the conductivity reduction were studied extensively in Ref. 23. Perhaps more important than the reduction in effective conductivity, is the appearance of isolated pebbles. Because heat deposition is volumetrically applied, pebbles with poor conduction routes become much hotter than their neighbors. This is evident in the high temperatures seen in many of the pebbles in the right figure of Fig. 3. Over-heating of isolated pebbles could induce sintering and impact their tritium release even when the average temperatures measured in the bed are well below sin-

(a) Well-packed bed
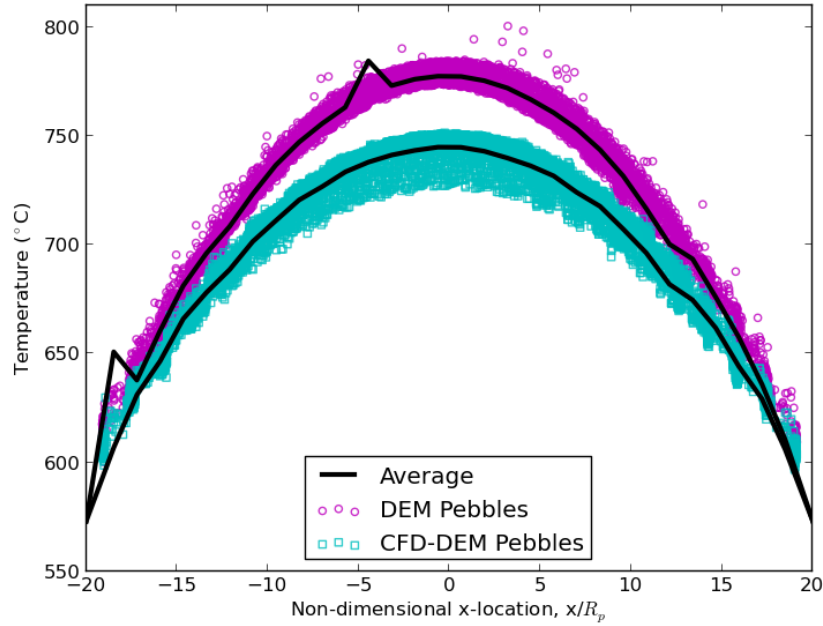
(b) Re-settled bed

Figure 6.3: Scatter temperature profiles of pebbles in a bed that is: well-packed (left) and resettled after 10% of pebbles were removed from crushing (right). The introduction of helium into the simulation contributes to both lower overall temperatures (higher effective conductivity) and the smoothing out of high temperatures of isolated pebbles.

tering values. When CFD-DEM beds are analyzed, there is still a large reduction in effective conductivity (22% drop), but interesting to note is the lack of isolated pebbles with high temperatures. In the CFD-DEM scatter plot of the right image in Fig. 3, there is evidence of the reduced heat transfer in the same region as the isolated pebbles from the DEM bed, but the temperatures are much closer to the average values of neighboring pebbles. The helium purge gas has effectively smoothed out the temperatures and provided heat transport paths for any pebbles that have loose physical contact with neighbors. In spite of the 22% decrease in effective conductivity, the maximum temperature of the pebble bed only increased 6.2% (from 725 to 751 K) when helium is included in the model. This result is significant for solid breeder designers. They may choose a solid breeder volume such that in the event of extensive pebble cracking, the maximum temperature of the bed would remain within the ideal windows dictate for the lithium ceramics.

Table 6.1: Pebble bed values from the test matrix of the beds analyzed in this study.

	k_{eff}		$T_{\max}$		$\frac{Q_h}{Q_{\text{nuc}}}$
	(W/mK)		(K)		
	DEM	CFD-DEM	DEM	CFD-DEM	CFD-DEM
Well-packed	0.96	1.09	745	725	1.15
Resettled	0.66	0.85	800	751	1.52

An accompanying result is the increased amount of energy carried out of the system by the helium purge gas. In Table I, the last column provides the ratio of energy carried out of the system to the nuclear energy deposited into the bed. The amount of energy carried out by the helium increased from 1.15% to 1.52% from 'well-packed' to 'resettled'. evap-x-T-color The CFD-DEM formulation maintains calculations of pebble-pebble interactions while dynamically coupling to the helium flow. The model demonstrates the ability of helium gas to smooth out any hot spots predicted by pure-conduction DEM formulations. Further, the lattice-Boltzmann simulation, while not fully coupled to DEM, revealed important features of helium flow in volumetrically heated pebble beds – mainly the smearing of temperature

profiles along the paths of cooling.

CHAPTER 7

Pebble Interaction Analysis: Experimental Relationships

Many experiments were carried out on individual ceramic pebbles. While there are some measures from experiments that are immediately useful for qualitative comparisons, such as the crush strength between different batches of ceramics, most values are not obviously connected to analysis of the pebbles nor the pebble bed assemblies they make up. In this section we will show had careful examination of single pebble experiments can lead to predictions of not only strength in ensembles but also modifications of the fundamental properties of the ceramic pebbles.

In section § 7.1, we use single pebble experiments to validate the use of Hertz theory for contacting ceramic pebbles, but also determine the proper Young's modulus to use for the ceramics. In section § 7.2 we use the theory we developed in section § **??** along with experimental data to begin to make predictions for survivability of pebbles in ensembles.

7.1   Elasticity reduction factor

We introduced Hertz theory in § **??**, and now we apply it to experiments for analysis of ceramic pebbles. The derivation of Hertz force can be found on page **??** but is given again here for reference.

$$F = \frac{4}{3} E^* \sqrt{R^*} \, \delta^{3/2}$$

and, again, the relative Young's modulus and radius are

$$\frac{1}{E^*} = \frac{1 - \nu_i^2}{E_i} + \frac{1 - \nu_j^2}{E_j}$$
$$\frac{1}{R^*} = \frac{1}{R_i} + \frac{1}{R_j}$$

In experiments where we press a ceramic pebble between two platens, we measure the travel, s, rather than the pebble overlap, so we modify Eq. **??** to be represented in terms of travel ($s = 2\delta$). Furthermore, for a pebble ($R_i = R_p$) in contact with a smooth plane ($R_j \to \infty$), the relative radius is simply $R^* = R_p = d_p/2$.

The Hertz force is now expressed as

$$F = \frac{1}{3}E^*\sqrt{d_p s^3} \tag{7.1}$$

Let's take a moment to discuss Eq. 7.1. The Young's modulus of the test stand platen is a constant value. One might assume the Young's modulus of the ceramic is also a known, constant value. In that case, there should be only a single force response for every pebble of a given diameter. Using the material properties given in Ref.[?] for Li_2TiO_3 , we plot a set of parametric curves based on diameter. The properties used for an nickel-alloy platen and Li_2TiO_3 are given in Table 7.1. The curves are given in Fig. 7.1.

Table 7.1: Material properties used for Li_2TiO_3 and nickel-alloy platen

E_{peb}	ν_{peb}	E_{stand}	ν_{stand}
(GPa)		(GPa)	
126	0.24	220	0.27

Figure 7.1 clearly shows that if a pebble of a given diameter is strictly obeying Hertz theory, there is only a single force-displacement curve it can follow. However, when experiments are performed on single pebbles we see quite different behavior for the F-s curves, see the curves of Fig. 7.2.
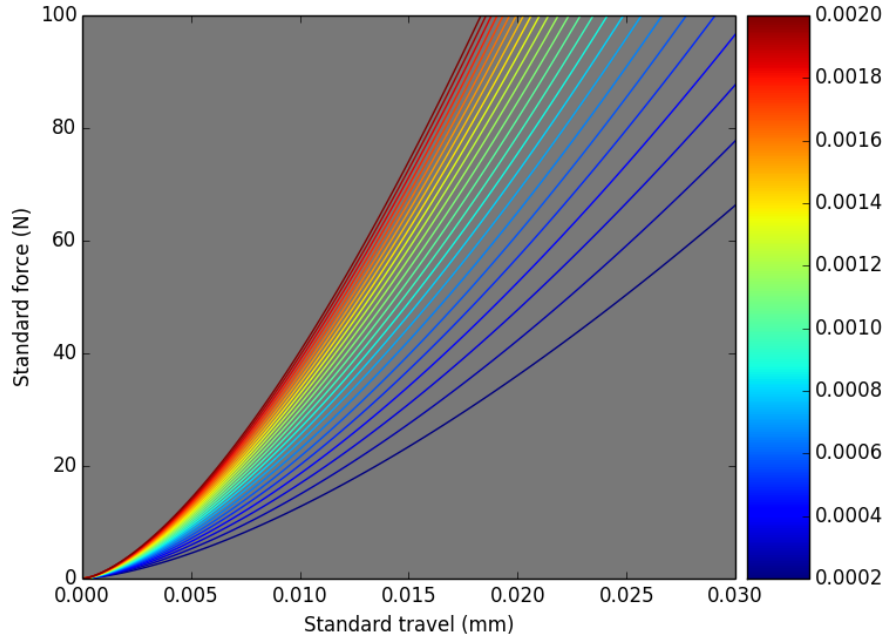
Figure 7.1: Hertzian responses of Li_2TiO_3 pebbles compressed between platens. The colormap shows pebble diameters in m. The diameters span an order of magnitude from $d_p = 0\,2$mm to $d_p = 2$mm.

Figure 7.2a shows Li_4SiO_4 pebbles as they are compressed between platens. Neglecting the handful of pebbles with very low force responses to high strain, there is a grouping of pebbles where there is a general trend that matches Fig. 7.1. The smaller diameter pebbles, in blue colors, have lower force responses for a given strain. Larger pebble diameters, in yellow-orange, are slightly higher overall in their force response. Finally, the largest diameter pebble in dark red has the highest force response for a given diameter. However, while the trends are *generally* similar to the theoretical Hertzian curves, there are noticeable spreads in responses. The responses of Li_2TiO_3 pebbles of Fig. 7.2b, on the contrary, show almost no adherence to the expected diameter dependence of Hertz theory.

The behavior of pebbles observed in Fig. 7.2 lead us to conclude that variations in pebble diameter can not alone account for the variation in the F-s curves. The most reasonable source for is a variation is in the Young's modulus of pebbles in a batch. Such a conclusion
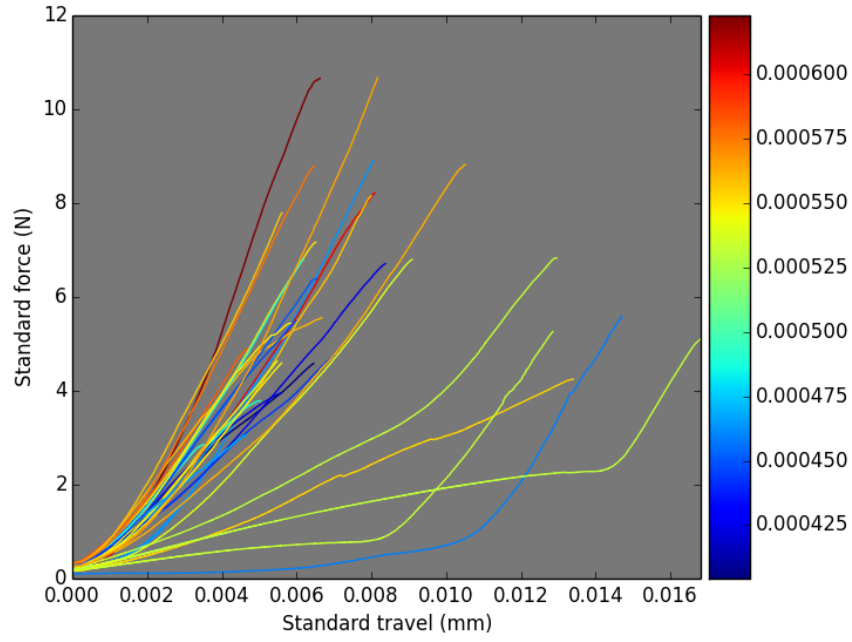
(a) Li$_4$SiO$_4$ pebbles of approximately 0 5mm diameter.
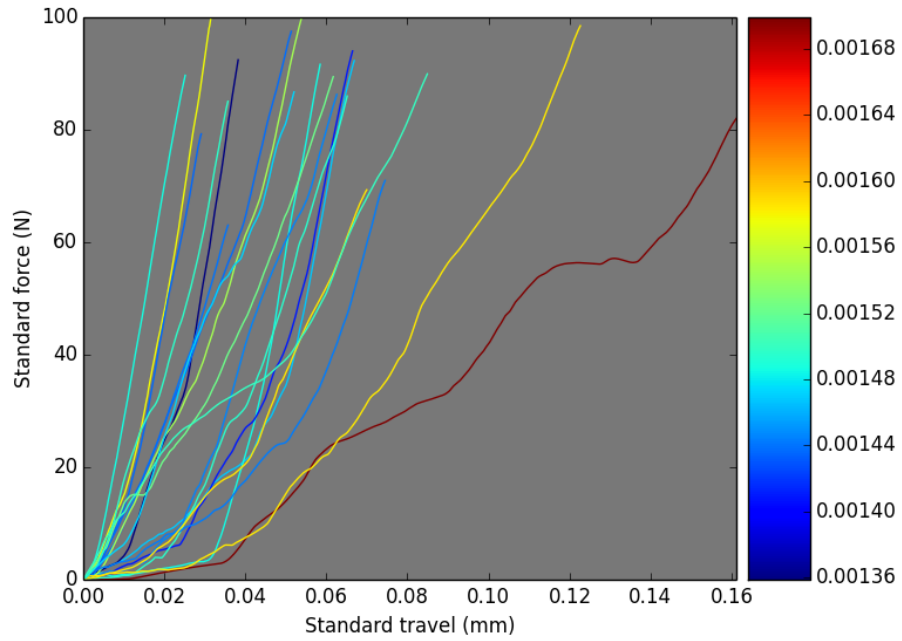
(b) Li$_2$TiO$_3$ pebbles of approximately 1 5mm diameter.

Figure 7.2: Force-displacement curves for two sets of experimental data, a batch of Li$_4$SiO$_4$ pebbles and a batch of Li$_2$TiO$_3$ pebbles. The colormap shows pebble diameters in m.

is important for implementation of Hertz theory in DEM algorithms.

We hypothesize that variation in the apparent Young's modulus of each pebble is rooted in the production of the pebbles which yields pebbles with slightly different internal structures. The differences in internal structure then cause the pebble to behave with different stiffnesses than the value expected from measurements of sintered pellets of lithium ceramics. In fact, we consider the sintered pellet Young's modulus, E_{sp}, as the upper limit for the pebbles and that most will emerge with values less than E_{sp}. To quantify the deviation of each pebble's E_{peb} from the sintered pellet, we introduce a k factor, defined as the elasticity reduction factor:

$$k = \frac{E_{peb}}{E_{sp}} \tag{7.2}$$

where

$$k \in [0, 1]$$

If each pebble has a unique k value, this would quantify the spread in elastic responses seen in the experiments. We find the value by assuming that the pebbles are, in fact, behaving in a Hertzian manner. This allows us to back-out a k value, or in other words the unique E_{peb} of that pebble by finding a best fit to the experimental curves.

We take the sintered pebble value of Young's modulus for Li_4SiO_4 to be $E_{sp} = 90$GPa and the value for Li_2TiO_3 to be $E_{sp} = 124$GPa. Then we iterate over all values of $k \in [0, 1]$ and compare the Hertzian response to that pebbles force-displacement curve. At each iteration, the L2-norm of the difference between Hertzian and experimental curves is used as the 'error'. The L2 norm, A for a given array, a is

$$||A||_F = \left[\sum_{i,j} \text{abs}(a_{i,j})^2 \right]^{1/2} \tag{7.3}$$

This is a convenient way to compare the error at every point along the force-displacement curves. When the error is minimized, the elasticity reduction value corresponding the minimum is recorded for that pebble. The Hertzian curves (in black) for each pebble are plotted in green against the experimental curves in Fig. 7.3.
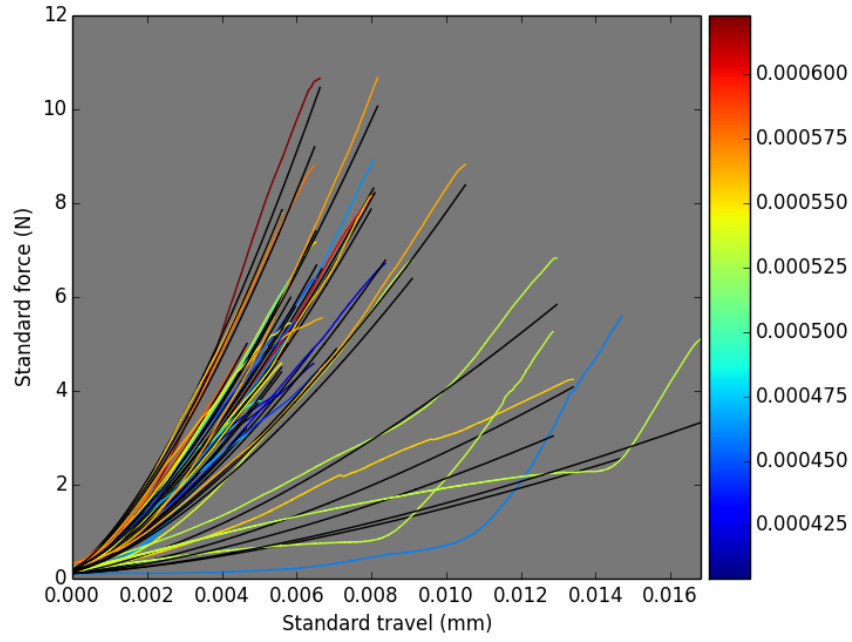
(a) Li$_4$SiO$_4$ pebbles of approximately 0 5mm diameter.
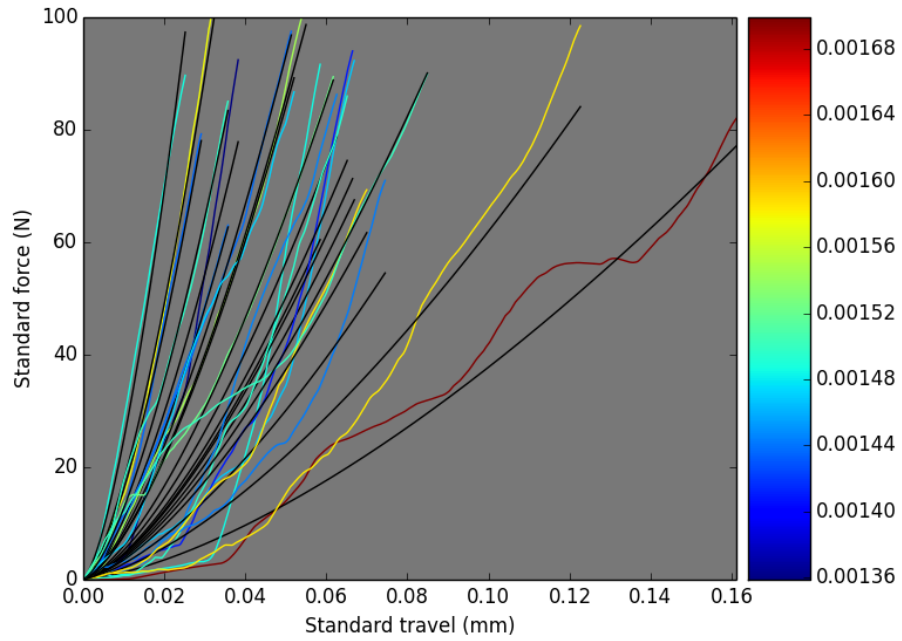
(b) Li$_2$TiO$_3$ pebbles of approximately 1 5mm diameter.

Figure 7.3: Force-displacement curves for two sets of experimental data, a batch of Li$_4$SiO$_4$ pebbles and a batch of Li$_2$TiO$_3$ pebbles. The colormap shows pebble diameters in m.

Many of the curves in Fig. 7.3a seem to be fit well with a Hertzian curve with modified Young's modulus. The value of Young's modulus found for each pebble is plotted in Fig. 7.4. The Young's modulus of pebble numbers 0 to 4 are the very 'soft' pebbles seen with very low forces on Fig. 7.3a. The majority of pebbles behave with a Young's modulus between 30 and 70 GPa. On the upper end, a few pebbles acted very similar to their sintered pellet counterpart with approximate value of 90GPa.

Figure 7.4: Distribution of modified Young's modulus for a batch of Li_4SiO_4 pebbles. Most pebbles responded to compression with a Young's modulus well below the sintered pellet value of 90GPa.

What remains is actually using these modified Young's modulus in DEM simulations to see if they more accurately reflect pebble bed macroscopic behavior. If so, it is assumed they will more accurately reflect the contact forces between pebbles in the ensemble.
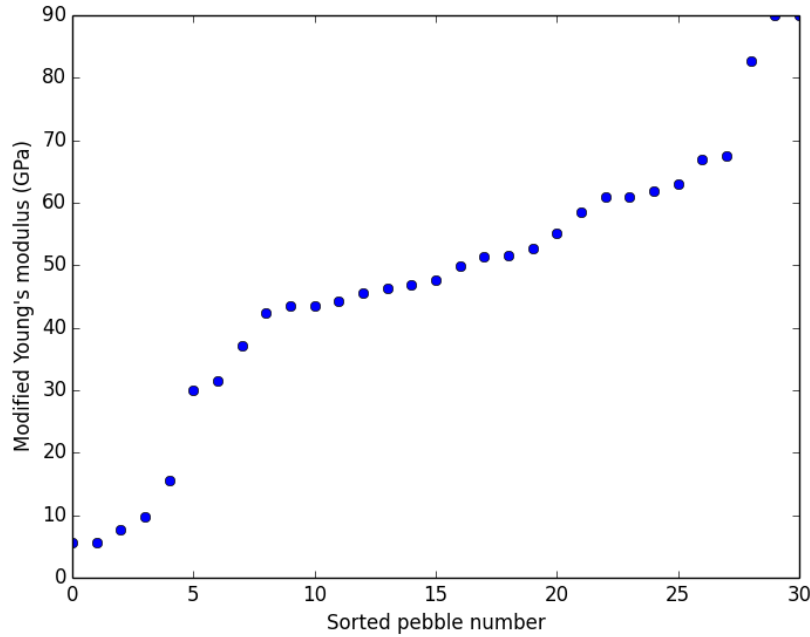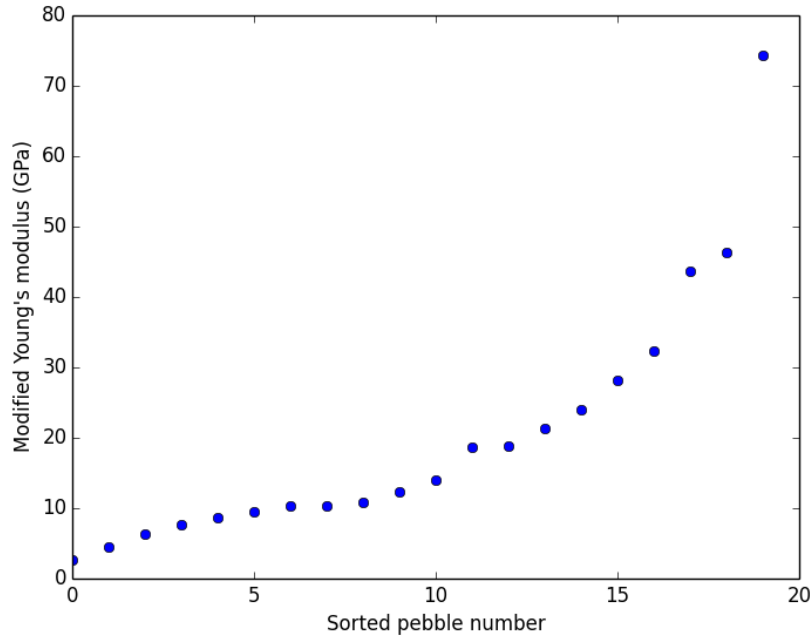
Figure 7.5: Distribution of modified Young's modulus for a batch of Li_2TiO_3 pebbles. All pebbles responded to compression with a Young's modulus well below the sintered pellet value of 126GPa.

7.2   Strain energy measurements

7.3   Linking interactions with strain energy

Hertz theory is applicable to any two contacting elastic objects. In practice, we cannot probe the contacts of small particles and rely on experiments where we press pebbles between flat platens. Here we will develop a theory for connecting the results of the experiments with the interaction of two spherical objects.

To relate the situation in the lab to two particles, we first integrate the Hertzian force along the overlap to find the strain energy, W_ϵ, of that contact.

$$W_\epsilon = \int_0^{\delta_c} F_n(\delta')\, \mathrm{d}\delta' \tag{7.4}$$

where the upper limit of the integration is the critical overlap δ_c (the meaning of this value

will be explained in detail later). With the force defined from Eq. **??**, this is straightforward to integrate.

$$W_\epsilon = \int_0^{\delta_c} \frac{4}{3} E^* \sqrt{R^*}\, \delta'^{3/2}\, \mathrm{d}\delta' \tag{7.5}$$

$$W_\epsilon = \frac{8}{15} E^* \sqrt{R^*}\, \delta_c^{5/2} \tag{7.6}$$

We will call the strain energy of the pebble compressed between platens as the lab strain energy, $W_{\epsilon,L}$. The strain energy of two particles in contact will be $W_{\epsilon,B}$. The assumption we make is that, if each interaction is integrated to the proper critical overlap, the strain energies will be equal at that point.

$$W_{\epsilon,L} = W_{\epsilon,B} = \frac{8}{15} E_B^* \sqrt{R_B^*}\, \delta_{c,B}^{5/2} \tag{7.7}$$

We solve for the interacting particle overlap as a function of the lab strain energy as

$$\delta_{c,B} = \left[\frac{15 W_{\epsilon,L}}{8 E_B^* \sqrt{R_B^*}} \right]^{2/5} \tag{7.8}$$

This overlap can be reinserted to Eq. **??** to find the critical force of the interacting particles as a function of the critical strain energy of the lab. Doing this, we find:

$$F_{c,B} = C E_B^{*\,2/5} R_B^{*\,1/5} W_{\epsilon,L}^{3/5} \tag{7.9}$$

where $C = \frac{4}{3} \left(\frac{15}{8} \right)^{3/5}$.

In this analysis we have referred to a 'lab' and 'particle' for the two situations. In fact, the result is more general and can be used to relate any two scenarios. The only requirement is that both conditions adhere to the assumptions of Hertz theory. The ramifications of this relationship will be explored in more detail in § **??**.

Sphere with heat generation

To provide homogeneous boundary conditions, the temperature will everywhere be in reference to its difference from the fluid temperature, i.e. $\mathbb{T} = T - T_f$.

Energy equation

$$\frac{1}{r}\frac{\partial^2}{\partial r^2}(r\mathbb{T}) + \frac{g}{k} = \frac{1}{\alpha}\frac{\partial \mathbb{T}}{\partial t} \tag{.10}$$

Subject to

$$\frac{\partial \mathbb{T}}{\partial r}\Big|_b + \frac{h}{k}\mathbb{T}\big|_b = 0 \tag{.11}$$

and

$$\mathbb{T}\big|_0 = \text{finite} \tag{.12}$$

with initial condition

$$\mathbb{T}(r, 0) = \mathbb{T}_0 \tag{.13}$$

Transform with

$$U(r, t) = r\mathbb{T}(r, t) \tag{.14}$$

Energy equation becomes

$$\frac{\partial^2 U}{\partial r^2} + \frac{gr}{k} = \frac{1}{\alpha}\frac{\partial U}{\partial t} \tag{.15}$$

Subject to

$$\frac{\partial U}{\partial r}\Big|_b + \left(\frac{h}{k} - \frac{1}{b}\right)U\big|_b = \frac{hb}{k}T_f \tag{.16}$$

and

$$U\big|_0 = 0 \tag{.17}$$

with initial condition

$$U(r, 0) = T_0 r \tag{.18}$$

Break up the problem into simpler problems

1. A set of steady-state problems defined by $U_{ss}(r)$

2. A homogeneous time-dependent problem defined by $U_h(r, t)$

The solution of U_{ss} is found from the solution of

$$\frac{\partial^2 U_{ss}}{\partial r^2} + \frac{gr}{k} = 0 \tag{.19}$$

subject to the boundary conditions of

$$U_{ss}\big|_0 = 0 \tag{.20}$$

$$\frac{\partial U_{ss}}{\partial r}\Big|_b + \left(\frac{h}{k} - \frac{1}{b}\right) U_{ss}\big|_b = 0 \tag{.21}$$

We separate and integrate,

$$\frac{\partial U_{ss}}{\partial r} = -\frac{g}{2k} r^2 + C_1 \tag{.22}$$

$$U_{ss} = -\frac{g}{6k} r^3 + C_1 r + C_2 \tag{.23}$$

The first boundary condition of Eq. .20 directly provides $C_2 = 0$. The second boundary condition is solved to give

$$C_1 = \frac{gb^2}{6k} \left(1 + \frac{2}{Bi}\right) \tag{.24}$$

valid for $Bi > 0$. Thus,

$$U_{ss} = \frac{gb^2}{6k} \left(1 + \frac{2}{Bi} - \frac{r^2}{b^2}\right) r \tag{.25}$$

We can now transform back to the temperature version of the equation with the simple reduction in power of r on U, $(U = r\mathbb{T})$,

$$\mathbb{T}_{ss} = \frac{gb^2}{6k}\left(1 + \frac{2}{Bi} - \frac{r^2}{b^2}\right) \tag{.26}$$

Now we non-dimensionalize with

$$\theta = \frac{\mathbb{T}}{gb^2/k} \tag{.27}$$

and

$$r^* = \frac{r}{b} \tag{.28}$$

$$\theta_{ss} = \frac{1}{6}\left(1 + \frac{2}{Bi} - r^{*2}\right) \tag{.29}$$

The next step is to find the homogeneous solution of

$$\frac{\partial^2 U_h}{\partial r^2} = \frac{1}{\alpha}\frac{\partial U_h}{\partial t} \tag{.30}$$

Subject to

$$U_h\big|_0 = 0 \tag{.31}$$

$$\frac{\partial U_h}{\partial r}\Big|_b + \left(\frac{h}{k} - \frac{1}{b}\right)U_h\big|_b = 0 \tag{.32}$$

and the initial condition of

$$U_{h,0} = \mathbb{T}_0 r - U_{ss} \tag{.33}$$

$$= \left[\frac{\mathbb{T}_0}{gb^2/k} - \frac{1}{6}\left(1 + \frac{2}{Bi} - \frac{r^2}{b^2}\right)\right]r \tag{.34}$$

We will again transform the spatial variable into a dimensionless form, $r^* = r/b$. The equation to solve is then,

$$\frac{\partial^2 U_h}{\partial r^{*2}} = \frac{b^2}{\alpha} \frac{\partial U_h}{\partial t} \tag{.35}$$

with boundary conditions of

$$U_h\big|_0 = 0 \tag{.36}$$

$$\frac{\partial U_h}{\partial r^*}\Big|_1 + (Bi - 1)U_h\big|_1 = 0 \tag{.37}$$

and an initial condition of

$$U_h(t = 0) = T_0 r^* b - \sum_{j=0}^{N} U_{0j} \tag{.38}$$

$$= \left[\frac{\mathbb{T}_0}{gb^2/k} - \frac{1}{6}\left(1 + \frac{2}{Bi} - r^*\right) \right] r^* b \tag{.39}$$

The solution is assumed of the form

$$U_h = R(r^*)\Gamma(t) \tag{.40}$$

The solution for Γ is given as

$$\Gamma = \exp(-\zeta^2 t/\tau) \tag{.41}$$

where $\tau = b^2/\alpha$. The space-variable function $R(\zeta, r^*)$ satisfies the following eigenvalue problem:

$$\frac{\mathrm{d}^2 R}{\mathrm{d}r^{*2}} + \zeta^2 R = 0 \tag{.42}$$

subject to

60

$$R = 0 \tag{.43}$$

at $r^* = 0$, and

$$\frac{\mathrm{d}R}{\mathrm{d}r^*} + (Bi - 1)R = 0 \tag{.44}$$

at $r^* = 1$. This eigenvalue problem is a special case of the Sturm-Liouville problem. The solution for U_h can be constructed from known eigenvalue solutions,

$$U(r,t) = \sum_{n=1}^{\infty} c_n R(\zeta_n, r^*) \exp(-\zeta^2 t/\tau) \tag{.45}$$

Application of the initial condition gives

$$F(r) = \sum_{n=1}^{\infty} c_n R(\zeta_n, r^*) \tag{.46}$$

where $F(r^*)$ is the initial condition we defined above,

$$F(r^*) = \left[\frac{\mathbb{T}_0}{gb^2/k} - \frac{1}{6}\left(1 + \frac{2}{Bi} - r^*\right) \right] \frac{gb^2}{k} r^* b \tag{.47}$$

The coefficients of c_n can be determined by applying the operator $\int_0^1 R(\zeta_n, r^*)\,\mathrm{d}r^*$ and utilizing the orthogonality property of eigenfunctions. The coefficients are found as

$$c_n = \frac{1}{N(\zeta_n)} \int_0^1 R(\zeta_n, r^{*\prime}) F(r^{*\prime})\,\mathrm{d}r^{*\prime} \tag{.48}$$

The norm, N is defined as

$$N(\zeta_n) = \int_0^1 [R(\zeta_n, r^*)]^2 \,\mathrm{d}r^* \tag{.49}$$

With the coefficients defined in Eq. .48, they can be substituted back into Eq. .45,

61

$$U(r^*, t) = \sum_{n=1}^{\infty} \exp(-\zeta^2 t/\tau) \frac{R(\zeta_n, r^*)}{N(\zeta_n)} \int_0^1 R(\zeta_n, r^{*\prime}) F(r^{*\prime}) \, dr^{*\prime} \tag{.50}$$

The eigenfunctions for Eq. .42 are

$$R(\zeta_n, r^*) = \sin(\zeta_n r^*) \tag{.51}$$

where the eigenvalues are the root of

$$\zeta_n \cot(\zeta_n) = -H \tag{.52}$$

and the normalization integral is given as

$$\frac{1}{N(\zeta_n)} = 2 \frac{\zeta_n^2 + H^2}{\zeta_n^2 + H^2 + H} \tag{.53}$$

where $H = (Bi - 1)$

In order to explicitly express the solution, we will first evaluate the integral

$$Z(\zeta_n) \frac{gb^2}{k} b = \int_0^1 R(\zeta_n, r^{*\prime}) F(r^{*\prime}) \, dr^{*\prime} \tag{.54}$$

$$= \int_0^1 \sin(\zeta_n r^{*\prime}) \left[\frac{\mathbb{T}_0}{gb^2/k} - \frac{1}{6} \left(1 + \frac{2}{Bi} - r^* \right) \right] r^* b \, dr^{*\prime} \tag{.55}$$

$$= \left\{ \left[\frac{\mathbb{T}_0}{gb^2/k} - \frac{1}{6} \left(1 + \frac{2}{Bi} \right) \right] \int_0^1 \sin(\zeta_n r^{*\prime}) r^{*\prime} \, dr^{*\prime} + \frac{1}{6} \int_0^1 \sin(\zeta_n r^{*\prime}) r^{*\prime 3} \, dr^{*\prime} \right\} \frac{gb^2}{k} b \tag{.56}$$

The two unique integrals are evaluated as

$$C_n = \int_0^1 \sin(\zeta_n r^{*\prime}) r^{*\prime} \, dr^{*\prime} = \frac{\sin \zeta_n - \zeta_n \cos \zeta_n}{\zeta_n^2} \tag{.57}$$

$$K_n = \int_0^1 \sin(\zeta_n r^{*\prime}) r^{*\prime 3} \, dr^{*\prime} = \frac{3(\zeta_n^2 - 2) \sin \zeta_n - \zeta_n(\zeta_n^2 - 6) \cos \zeta_n}{\zeta_n^4} \tag{.58}$$

Thus

$$Z(\zeta_n) = \left[\frac{T_0}{gb^2/k} - \frac{1}{6}\left(1 + \frac{2}{Bi}\right)\right] C_n + \frac{1}{6}K_n \qquad (.59)$$

or in terms of our dimensionless temperature,

$$Z(\zeta_n) = \left[\theta_0 - \frac{1}{6}\left(1 + \frac{2}{Bi}\right)\right] C_n + \frac{1}{6}K_n \qquad (.60)$$

The solution in terms of the transformed variable, $U(r^*, T)$ is now written as

$$U(r^*, t) = \sum_{n=1}^{\infty} \exp(-\zeta^2 t/\tau)\sin(\zeta_n r^*)\frac{Z(\zeta_n)\frac{gb^2}{k}b}{N(\zeta_n)} \qquad (.61)$$

Now we can write the solution for $\mathbb{T}(r^*, t)$ direclty from $U(r^*, t)$,

$$\mathbb{T}(r^*, t) = \sum_{n=1}^{\infty} \exp(-\zeta^2 t/\tau)\frac{\sin(\zeta_n r^*)}{r^*}\frac{Z(\zeta_n)\frac{gb^2}{k}}{N(\zeta_n)} \qquad (.62)$$

With one last step, we introduce the dimensionless temperature defined from Eq. .27

$$\theta(r^*, t)_{t.g.} = \sum_{n=1}^{\infty} \exp(-\zeta^2 t/\tau)\frac{\sin(\zeta_n r^*)}{r^*}\frac{Z(\zeta_n)}{N(\zeta_n)} \qquad (.63)$$

For comparison, we will non-dimensionalize the heat transfer as:

$$Q^* = \frac{Q}{Q_\infty} \qquad (.64)$$

where Q_∞ is the maximum possible amount of energy transfer between the solid and fluid. This value is equal for both lumped capacitance and the exact solution and is:

$$Q_\infty = -\rho_r C_r V(T_f - T_i) \qquad (.65)$$

Introducing this non-dimensional heat transfer term and the energy balance is expressed as:

$$Q^*_{t.g.} = \int \frac{-\rho_r C_r \big(T(r,t) - T_0\big) dV}{-\rho_r C_r V (T_\infty - T_0)} \qquad (.66)$$

$$Q^*_{t.g.} = \frac{1}{V} \int 1 - \theta_{t.g.} \, dV \qquad (.67)$$

For a circle in spherical coordinates:

$$dV = r^2 \sin(\phi) dr d\phi d\theta \qquad (.68)$$

In non-dimensional terms and assuming only a radial dependence, this becomes:

$$dV = 4\pi R^3 r^{*2} dr^* \qquad (.69)$$

The exact equation for dimensionless heat transfer for a sphere is then:

$$Q^*_{t.g.} = \frac{4\pi R^3}{V} \int_0^1 \left[1 - \sum_{n=1}^{\infty} \exp(-\zeta^2 t/\tau) \frac{\sin(\zeta_n r^*)}{r^*} \frac{Z(\zeta_n)}{N(\zeta_n)} \right] r^{*2} \, dr^* \qquad (.70)$$

This reduces to:

$$Q^*_{t.g.} = 1 - 3 \sum_{n=1}^{\infty} \exp(-\zeta^2 t/\tau) \frac{Z(\zeta_n)}{N(\zeta_n)} \int_0^1 r^* \sin(\zeta_n r^*) \, dr^* \qquad (.71)$$

And we recognize the integral as one which we solved previously,

$$Q^*_{t.g.} = 1 - 3 \sum_{n=1}^{\infty} \exp(-\zeta^2 t/\tau) \frac{Z(\zeta_n)}{N(\zeta_n)} C_n(\zeta_n) \qquad (.72)$$

And we are left with a formula for the total heat removed from the sphere as only a function of the eigenvalues and time.